Stress-induced nucleoid remodeling in Deinococcus radiodurans is associated with major changes in Heat Unstable (HU) protein dynamics

Pierre Vauclare, Jip Wulffelé, Françoise Lacroix, Pascale Servant, Fabrice Confalonieri, Jean-Philippe Kleman, Dominique Bourgeois, Joanna Timmins

Nucleic Acids Research, 2024, **52**, 6406–6423
https://doi.org/10.1093/nar/gkae379
Advance access publication date: 14 May 2024
Genome integrity, repair and replication

Stress-induced nucleoid remodeling in *Deinococcus radiodurans* is associated with major changes in Heat Unstable (HU) protein dynamics

Pierre Vauclare[1,†], Jip Wulffelé[1,†], Françoise Lacroix[1], Pascale Servant[2], Fabrice Confalonieri[2], Jean-Philippe Kleman[1], Dominique Bourgeois[1,*] and Joanna Timmins[1,*]

[1]Univ. Grenoble Alpes, CNRS, CEA, IBS, F-38000 Grenoble, France
[2]Université Paris-Saclay, CEA, CNRS, Institute for Integrative Biology of the Cell (I2BC), 91198 Gif-sur-Yvette, France

[*]To whom correspondence should be addressed. Tel: +33 457428678; Email: joanna.timmins@ibs.fr
Correspondence may also be addressed to Dominique Bourgeois. Email: dominique.bourgeois@ibs.fr
[†]The first two authors should be regarded as Joint First Authors.

Abstract

Bacteria have developed a wide range of strategies to respond to stress, one of which is the rapid large-scale reorganization of their nucleoid. Nucleoid associated proteins (NAPs) are believed to be major actors in nucleoid remodeling, but the details of this process remain poorly understood. Here, using the radiation resistant bacterium *D. radiodurans* as a model, and advanced fluorescence microscopy, we examined the changes in nucleoid morphology and volume induced by either entry into stationary phase or exposure to UV-C light, and characterized the associated changes in mobility of the major NAP in *D. radiodurans*, the heat-unstable (HU) protein. While both types of stress induced nucleoid compaction, HU diffusion was reduced in stationary phase cells, but was instead increased following exposure to UV-C, suggesting distinct underlying mechanisms. Furthermore, we show that UV-C-induced nucleoid remodeling involves a rapid nucleoid condensation step associated with increased HU diffusion, followed by a slower decompaction phase to restore normal nucleoid morphology and HU dynamics, before cell division can resume. These findings shed light on the diversity of nucleoid remodeling processes in bacteria and underline the key role of HU in regulating this process through changes in its mode of assembly on DNA.

Graphical abstract

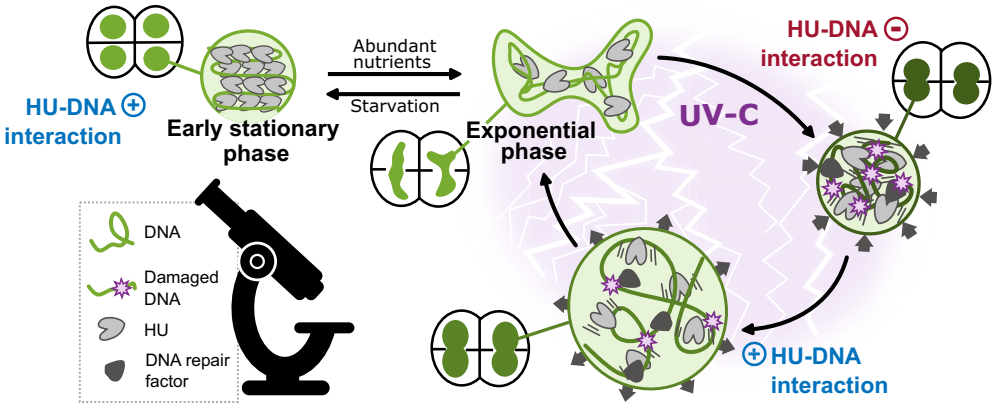

Introduction

An organism's capacity to survive depends largely on its ability to sense and respond to changes in its environment. This is particularly true for bacteria that are constantly exposed to adverse environmental conditions, affecting their physiology, growth and survival. To respond to such stress, bacteria have developed a wide range of strategies. Among these, large-scale reorganization of the overall architecture of the genome appears to be one of the most rapid and effective, especially in response to sudden stress (1,2), and is generally associated with temporal changes in the gene expression profile of the bacterium (3–6). Stress-induced nucleoid remodeling is a widespread mechanism shared across many bacterial species including human pathogens and often results in a more compact nucleoid. It typically occurs in bacteria entering stationary phase or undergoing sporulation (1,7–9), states in which bacteria can withstand major changes in their environment, such as reduced nutrient availability (10,11). Nucleoid remod-

Received: December 15, 2023. **Revised:** April 23, 2024. **Editorial Decision:** April 24, 2024. **Accepted:** April 26, 2024

eling has also been reported in bacteria exposed to antibiotics, low pH, or oxidative stress (2,6,12,13). Nucleoid condensation has been proposed to insulate genomic DNA from its environment by creating a physical barrier between the genome and the stress factors (2,14), and to facilitate DNA repair by limiting the diffusion of broken chromosomes (15). Despite the well-recognized importance of nucleoid remodeling as a major response to stress, the molecular mechanisms underlying this reorganization remain poorly understood.

The bacterial nucleoid displays a highly hierarchical organization, composed of macro- and micro-domains that play key roles in genome maintenance and regulation of gene expression (1,9). This packaging of the genome is achieved by several factors, including DNA supercoiling, molecular crowding and the abundant nucleoid-associated proteins (NAPs). NAPs are small positively charged proteins that interact with the genomic DNA to define the architecture of the nucleoid. NAPs preferentially bind to DNA in a non-specific manner and control DNA packaging through DNA bending, wrapping or bridging distant strands. However, they have also been reported to bind specifically to DNA motifs, thereby contributing to regulating processes such as gene-specific transcription, replication, recombination and repair (1,16,17). A large number of genes involved in bacterial viability, metabolism and stress response are thus directly or indirectly regulated by NAPs (6,18,19). Environmental changes have been shown to affect the expression level and/or DNA binding properties of NAPs, notably through post-translational modifications such as phosphorylation, acetylation, methylation, succinylation, oxidation and deamination, in turn affecting the DNA topological organization (20–23). In many bacteria, NAPs and in particular Dps (DNA-binding protein from starved cells) proteins have been shown to contribute to nucleoid condensation and DNA protection, notably in stationary phase (24–28). NAPs are thus likely to be key players in stress-induced nucleoid remodeling (29,30).

Most of our current knowledge on nucleoid organization comes from the study of rod-shaped bacteria like *Escherichia coli*, while studies on cocci are still sparse. A fascinating model is the well-known *Deinococcus radiodurans*, a non-pathogenic gram-positive coccus (31,32). The exceptional resistance of *D. radiodurans* to a wide range of genotoxic stresses including desiccation, oxidizing agents, and ionizing and UV radiation, has been attributed to its effective anti-oxidant and reactive oxygen species (ROS)-scavenging strategies combined with a highly efficient DNA repair machinery (33,34). This outstanding resilience makes *D. radiodurans* particularly relevant for investigating microbial responses to space conditions (radiation, desiccation, vacuum, extreme temperature) and is sparking considerable interest in its potential applications in space exploration (35–37). *D. radiodurans* possesses a complex multipartite and multicopy genome arranged into a condensed nucleoid (8,15). Interestingly, it was shown that *D. radiodurans* nucleoids remain nonetheless highly dynamic, capable of adopting multiple distinct structures in exponential phase as cells progress through their cell cycle (8). Strikingly, in comparison with radiosensitive bacteria (18), the high level of chromosome compaction in *D. radiodurans* is managed by a small number of versatile NAPs (38,39). Indeed, amongst the five most abundant NAPs found in *E. coli* (HU, IHF, H-NS, Fis and Dps), only two of them, HU and two Dps variants (Dps1 and Dps2), are present in *D. radiodurans* (31,40,41). These two Dps proteins, however, do not appear to play a major role in nucleoid organization and condensation as observed in *E. coli*, but have instead been shown to contribute to protection against oxidative stress by regulating the availability of manganese and iron in the cell (42–44). Moreover, the Hfq regulon that has been proposed to contribute to nucleoid packaging in bacteria (28,45), is also missing in *D. radiodurans*.

The ubiquitous histone-like HU protein is the most widespread and abundant NAP in bacteria (46). Extensive studies have shown that HU is a dimeric protein that exists mostly as a homodimer, but also as a heterodimer in enterobacteria such as *E. coli*, where it can form either homo- (HUα-HUα) or heterodimers (HUα-Huβ) (42,47,48). In spore-forming bacteria, HU is encoded by a single gene in *Bacillus* spp. (*HBsu*) and assembles exclusively as a homodimer, while *Streptomyces* genomes carry two distinct genes (*hupA* and *hupS*) (9,49,50). HupA is a conventional HU protein similar to the heterodimers (HUα/Huβ) found in *E. coli* and is expressed during vegetative growth. HupS, in contrast, is specifically expressed during sporulation and is associated with nucleoid condensation within mature spores (9,49). The role of HU in nucleoid compaction appears multifold. Recent single-particle tracking experiments have suggested that HU mainly contributes to nucleoid organization via transient non-specific interactions (51,52). At the same time, *in vitro* studies have shown that HU exhibits both non-specific binding to unstructured DNA and higher affinity specific binding to distorted DNA structures (53–55). HU is also able to multimerize on DNA, leading to DNA stiffening or compaction depending on its concentration (6,39,48). HU-DNA interactions have indeed been proposed to be affected by the local HU concentration, but also by post-translational modifications, in particular phosphorylation and acetylation, which contribute to the fine tuning of the global architecture of the nucleoid (20,21,23,56). Beyond its role in nucleoid organization, HU, like other NAPs, has been reported to play a role in transcriptional regulation, DNA replication and DNA repair (53,57–59). HU-deficient *E. coli* cells remain viable with a modest change in phenotype, but have been found to be more sensitive to UV irradiation (60), suggesting a role for HU in bacterial stress-response.

In *D. radiodurans*, unlike in *E. coli*, the *hbs* gene encoding HU is essential for cell viability, and the progressive depletion of *D. radiodurans* HU (DrHU) using a thermosensitive plasmid leads to nucleoid decondensation, fractionation and eventually cell lysis (42). Together with the DNA gyrase that modulates the topology of the genomic DNA, DrHU thus appears to be the primary structuring protein orchestrating nucleoid organization in *D. radiodurans* (61). Interestingly, DrHU harbors an additional 30 amino acid long N-terminal lysine-rich extension, that is reminiscent of the C-terminal domain of eukaryotic histone H1, which is also involved in DNA compaction (61,62).

In this work, using notably a combination of 3D spinning-disk microscopy and single-particle tracking experiments, we have performed an in-depth study of nucleoid remodeling in *D. radiodurans* and its associated changes in HU dynamics, induced by two types of stress: (i) entry into stationary phase, a stress that occurs frequently in the natural environment, during which bacteria are faced with resource-limited conditions preventing any further growth (63,64), and (ii) exposure to intense UV-C light that produces extensive DNA damage, and notably the formation of pyrimidine photoproducts, but also ROS (65). The data reveal that the nucleoid adopts a

compacted and spherical morphology both in stationary phase and immediately after exposure to UV-C radiation. However, strikingly, single-particle tracking of HU revealed that while HU diffusion decreases during stationary phase, it dramatically increases following exposure to UV-C, suggesting that the underlying mechanisms are distinct. Furthermore, by comparing the cellular response of *D. radiodurans* to sublethal and lethal doses of UV-C light, we determined that the nucleoid remodeling process starts with a rapid nucleoid condensation step associated with increased HU diffusion, which is then followed by a slower decompaction phase, seen only in surviving cells, during which genome integrity and nucleoid organization are restored before DNA replication and cell growth can resume. Together, these findings highlight the key role of HU in stress-induced nucleoid remodelling, but also the complexity of this phenomenon in bacteria.

Materials and methods

Bacterial cultures

Bacterial strains used in this study are listed in Supplementary Table S1 and illustrated schematically in Supplementary Figure S1. All *D. radiodurans* strains were derivatives of the wild-type strain R1 ATCC 13939 (DR^{WT}). The genetically engineered strain of *D. radiodurans* expressing HU fused to mEos4b (GY16993; DR^{HUmEos}) was obtained by the tripartite ligation method (66). For this, a codon-optimized gene encoding mEos4b to which we added the 9 N-terminal residues of mCherry was synthesized and subloned into plasmid pEX-128 by Eurofins MWG Biotech (Supplementary Figure S1). Obtaining a viable and functional strain of *D. radiodurans* expressing HU fused to a fluorescent protein is not trivial. Since we knew that mCherry fusions were functional, we decided to add the extra N-terminal residues of mCherry to the N-terminus of mEos4b. We inserted a hygromycin resistance (*hph*) cassette into the AgeI/XbaI sites of pEX-128 downstream of the mEos4b gene, then amplified the mEos4bΩ*hph* cassette and the regions flanking the insertion site (3′ end of *hu* gene, DR_A0065) by PCR using oligonucleotides listed in Supplementary Table S2, and after restriction digestion the three fragments were ligated together. *D. radiodurans* cells were then transformed by the ligation product and plated on selective medium containing 50 μg/ml hygromycin, leading to allelic replacement on one genome copy. Because *D. radiodurans* is multigenomic, the transformant colonies were further streaked three times successively on selective medium to ensure that all copies of the genome had incorporated the foreign DNA. This was then confirmed by PCR analysis and DNA sequencing, which also revealed a point mutation in mEos4b (Ala^{112} to Val^{112}). *D. radiodurans* cells were grown aerobically at 30°C in a shaking incubator (160 rpm) in Tryptone-Glucose-Yeast extract 2x (TGY2X) medium supplemented with the appropriate antibiotics: 3.4 μg/ml chloramphenicol for DR^{HUmCh} GY15743 strain and *oriC*/*ter* labelled strains GY15787 and GY15800, and 50 μg/ml hygromycin for DR^{HUmEos} GY16993. Typically for microscopy experiments, *D. radiodurans* cells were pre-grown the day before and then diluted for an overnight growth until reaching exponential ($OD_{650} \sim 0.3$–0.5) or early stationary phase ($OD_{650} > 3$) the next morning. *oriC*/*ter* labelled strains GY15787 and GY15800 were grown overnight and were diluted 60X the next morning in TGY2X and grown for a further 5h until reaching an OD_{650} between 0.3 and 0.5. *Escherichia coli* strain DH5α was grown at 37°C in LB medium. Optical density measurements were made on a Clariostar (BMG Labtech) plate reader.

UV irradiation and survival curve

Before irradiation, cells were washed two times with minimal medium M9DR (45.5 mM Na_2HPO_4, 22 mM KH_2PO_4 and 15.1 mM $(NH_4)_2SO_4$, pH7.3) to eliminate the strongly UV-absorbing TGY2X medium. Cells were finally resuspended in M9DR medium at an OD_{650} between 0.3 and 0.5 and transferred to a 6-well plate (1 ml per well). Cells were irradiated at a low cell density and in a minimal volume to ensure a homogeneous exposure of the cells. UV-C (254nm) irradiation was performed using a Stratalinker oven equipped with germicide UV-C lamps producing a continuous dose of $\sim 30 J/m^2/s$. Cells were typically irradiated between 0.5 and 5 minutes. The exact dose received by the cells was determined using a UV-C light monitor placed next to the 6-well plate in the UV oven. Exposure to UV-C irradiation led to a small reduction in the fluorescence of the fluorescent proteins (Supplementary Figure S2A). After irradiation, cells were centrifuged and resuspended in fresh TGY2X medium. For the recovery experiments, these cultures were returned to the 30°C shaking incubator. Samples were collected immediately after resuspending cells in TGY2X medium (t_0) and then 1, 2, 3, 5, 7, 9 and 24 h post-irradiation (for the confocal analysis) or 1, 3, 6 and 24 h post-irradiation (for the spt analysis). OD_{650} measurements were made every hour on three independent cultures for 9h post-irradiation and then the following day (t_{24h}). Full UV-C survival curves were performed for *E. coli* DH5α and exponential and stationary phase DR^{WT} by serially diluting non-irradiated and irradiated cultures (exposed to 0 to 12 kJ/m^2 for DR^{WT} or 0 to 0.95 kJ/m^2 for *E. coli*) and spotting 8 μl of each dilution on TGY1X or LB (for *E. coli*) agar plates. After 48h incubation of the plates at 37°C, individual colonies were counted and the surviving fraction was determined using non-irradiated cells as a reference. A similar procedure was used to determine the survival fraction of $DR^{HU\text{-}mCh}$ and $DR^{HU\text{-}mEos}$ strains after exposure to 1.9 and 12.0 kJ/m^2.

Sample preparation for confocal microscopy and sptPALM

For confocal microscopy analysis, DR^{WT} cells were stained with Nile Red (30 μM) and Syto9 (200 nM) for 10 min at room temperature, to visualize the cell membrane and nucleoid, respectively, while DR^{HUmCh} cells were only stained with syto9 (200 nM). The cells were then harvested by centrifugation and resuspended in 10 μl TGY2X. 0.5 μl of this cell suspension was then placed on a 1.5% (w/v) low melting agarose (LMA; Bio-Rad) TGY2X pad prepared on a cover glass using a gene frame (Thermo Scientific). A 2 mm-wide band of LMA was cut out to provide oxygen. A glass slide was then placed on top of the pad and the sample was sealed with picodent Twinsil®. Sample preparation for microscopy typically took approximately 30 min, so cells were usually imaged 30 min after the designated timepoint. The samples were maintained at 30°C during image acquisition. For spt analysis, cells were washed 3 times in M9DR medium to limit autoblinking, as described previously (67), and were finally resuspended in 20–100 μl M9DR medium, depending on the

size of the pellet. 10 μl of this cell suspension was then placed on a coverslip cleaned with an ozone cleaner device (UVOCS) and the cells were left to sediment for 2 minutes, after which the excess liquid was removed. After a further 2–4 min of air-drying, 10 μl 1.5% (w/v) LMA in M9DR was poured over the cells and a glass slide was placed on top to evenly distribute the LMA. Samples were sealed with picodent Twinsil® and imaged within 20 min.

Confocal data acquisition

Spinning-disk confocal microscopy was performed using an Olympus IX81 inverted microscope equipped with a Yokogawa CSU-X1 confocal head. The excitation laser beam (Ilas2 laser bench, GATACA systems) was focused to the back focal plane of a 100× 1.49-numerical-aperture (NA) oil immersion apochromatic objective. For cell and nucleoid analyses, series of Z-planes were acquired every 100 nm using a PRIOR N400 piezo stage. Fluorescence excitation was performed at 488 nm for Syto 9 and 561 nm for Nile Red or mCherry. Fluorescence emission was collected with an Andor iXon Ultra EMCCD camera through a quad-band Semrock™ Di01-T405/488/568/647 dichroic mirror and single-band emission filters adapted to each fluorophore used: 520 nm for Syto9 (FF02-520/28 Semrock™), and 600 nm for mCherry or Nile Red (ET600/50m Chroma™). Data acquisition was performed using Metamorph 7.10 (Molecular devices).

SptPALM data acquisition and tracking of *oriC*/*ter* loci

SptPALM acquisitions on the DR^{HumEos} strain were acquired on a SAFE 360 (Abbelight) SMLM set up. Data was acquired at 27°C under continuous illumination with 400 W/cm^2 561 nm light and a frame time of 10 ms. The intensity of the 405 nm laser was manually increased during acquisition to maintain approximately constant localization density. 40 000–60 000 frames were acquired per dataset. A transmission light image was acquired prior to sptPALM acquisition for segmentation of the cells. *oriC* and *ter* labeled strains of *D. radiodurans* were imaged on a home-built PALM set-up. First, a bright field image and an image of HU-mCherry were collected (100 ms exposure time, 10 W/cm^2 561 nm light). Second, the *oriC* or *ter* sites labelled with ParB-GFP were imaged every second using an exposure time of 100 ms and 10 W/cm^2 488 nm light, until all sites had bleached (∼100–500 frames).

Confocal data analysis

3D nucleoids were segmented by automatic thresholding of the Syto9 or mCherry fluorescence signal using the 'surface' procedure of the Imaris software (Oxford instruments) after parameter optimization (surface smoothing detail = 0.1 μm and background subtraction = 0.2 μm). The volume, sphericity and mean channel intensities (in the two channels) of the segmented nucleoids were then extracted for further analysis. After exposure to sublethal and lethal doses of UV-C light, 450–550 individual cells from each timepoint (t_0 to t_{24h}) were classified in terms of phase of the cell cycle (phase P1 to P6 for exponentially growing cells and phases P1 to P8 for stationary cells), cell perimeter, cell integrity, nucleoid volume, nucleoid morphology and nucleoid position (centered or off-center). Cell perimeters were obtained by automatic segmentation of cells using Cellpose (68) and conversion of the obtained masks into ROIs in Fiji (69), which could be used to extract the perimeter of the segmented cells. Phase 5 cells, in particular, but also some distorted cells were poorly segmented by Cellpose. In these cases, segmentation was performed manually in ImageJ.

sptPALM and oriC/ter tracking data analysis

Nucleoids were manually segmented from an overlay of the bright field and super-resolved images of HU-mEos4b. A small fraction of cells with poorly defined nucleoids were excluded from further analysis. Despite the washing steps, occasionally a fraction of cells still showed strong autoblinking (67); these cells were also discarded from the analysis. Single molecules were localized using the ThunderSTORM plugin in ImageJ (70). Trajectories of single molecules were obtained using the tracking software Swift (Endesfelder *et. al.*, in prep.), using the following tracking parameters: 'exp_displacement = 60 nm', 'p_bleach = 0.1', 'p_blink = 0.2', 'p_reappear = 0.5', 'precision = 22 nm', 'max_displacement = 250 nm', 'max_displacement_pp = 250 nm' and 'max_blinking_duration = 2 frames'. Default values were used for the other parameters. Swift splits tracks, which contain motion changes (i.e. immobile → diffusive), into segments containing unique behaviors. These segments were considered as trajectories for further analysis. Of note, only a small fraction of the tracks of HU-mEos4b contained multiple segments (∼1–2%) suggesting that the time HU-mEos4b spends in a given state is relatively long compared to the average track length.

Trajectories were further analyzed in MATLAB to assign them to specific nucleoid morphologies based on the applied segmentation and to calculate the apparent diffusion coefficients. Apparent diffusion coefficients of single trajectories (Di*) were calculated from the mean squared jump distance as described by Stracy *et al.* (52) using:

$$D_i^* = \frac{1}{4n\Delta t}\sum_{i=1}^{n}[x(i\Delta t) - x(i\Delta t + \Delta t)]^2 + [y(i\Delta t) - y(i\Delta t + \Delta t)]^2$$

where n is the number of displacements over which the mean squared jump distance is calculated, $x(t)$ and $y(t)$ are the coordinates of the molecule at time t and Δt is the frametime. In this work, 4 displacements per track (made of at least 5 measurements) were taken into account ($n = 4$).

OriC and *ter* loci were localized using ThunderSTORM (70). Trajectories were obtained using Swift (Endesfelder, M. *et. al.*, in preparation) with the following tracking parameters: 'exp_displacement = 50 nm', 'p_bleach = 0.001 ', 'precision = 50 nm', 'max_displacement = 250 nm', 'max_displacement_pp = 250 nm'. Default values were used for the other parameters. Trajectories were further analyzed in MATLAB to calculate the apparent diffusion coefficients. Only trajectories with > 10 localizations were considered.

Western blot analysis

Triplicate 10 ml samples of non-irradiated and irradiated (at t_{1h} after exposure to sublethal UV-C) exponential phase DR^{WT}, DR^{HUmCh} and DR^{HUmEos} cultures and 5 ml samples of non-irradiated stationary phase cultures were collected for western blot analysis of the HU expression. Each culture was resuspended in 0.2 ml PBS supplemented with protease

inhibitors (Roche), DNaseI (Roche) and lysozyme (Roche). Cell suspensions were lysed by two 10-s sonications with a microtip followed by 45 min mechanical shaking with 100 µl glass beads (Macherey Nagel) at 4°C. Cell debris were eliminated by centrifugation at 14000 rpm for 10 min and the soluble fraction was recovered. 4 µg of each cell extract was loaded on a 12% stain-free SDS-PAGE gel (BioRad), alongside purified HU, HU-mCherry and HU-mEos4b as described previously (39), and separated by gel electrophoresis at 175 V for 45 min, before transferring the bands to a nitrocellulose membrane using the BioRad transblot system. A stain-free image of the blot was acquired at this point for normalization of the lanes before blocking the membrane with 3% BSA in PBS for 60 min. The membrane was then incubated overnight at 4°C with either a mouse monoclonal anti-mCherry antibody (Origene; 1:1500) diluted in 5% milk in PBS, a rabbit polyclonal anti-HU antibody (1:500) diluted in 3% BSA in PBS, or both antibodies diluted in 3% BSA in PBS. After five washes with PBS supplemented with 0.02% Tween20 (PBS-Tween), the membrane was further incubated for 2 h at 25°C with a second antibody (anti-mouse conjugated to StarBright B700 or anti-rabbit conjugated to StarBright B520 from Bio-Rad or both) diluted 1:2500 in PBS-Tween. After five additional washes with PBS-Tween, the fluorescently labeled bands were visualized on a Chemidoc MP imager (BioRad) using appropriate excitation/emission parameters and quantified using ImageLab (BioRad). The total amount of protein loaded in each lane was normalized using the stain-free image. All samples were prepared in triplicate and the mean and standard deviation of the obtained values were plotted in GraphPad Prism 8.

Statistical analysis

Large datasets (e.g. nucleoid volume, sphericity, D_{app}) were analyzed using non-parametric Kruskal–Wallis statistical tests in GraphPad Prism 8, while triplicate measurements of HU abundance and fluorescence intensity before and after exposure to UV-C light were analyzed using ordinary one-way ANOVA (uncorrected Fisher's LSD) statistical tests in GraphPad Prism 8. Two-tailed P values <0.05 were considered as significant and were indicated with asterisks: ns: non-significant, * $P \leq 0.05$, ** $P \leq 0.01$, *** $P \leq 0.001$, **** $P \leq 0.0001$.

Results

Entry into stationary phase induces nucleoid compaction associated with decreased HU dynamics

In our previous work, we characterized the size and morphology of *D. radiodurans* nucleoids, revealing a great diversity of nucleoid shapes in exponential growth phase and more condensed and homogeneous nucleoids in stationary phase (8). We confirmed these findings by 3D spinning-disk microscopy imaging of membrane (Nile Red)- and DNA (Syto9)-stained wild-type *D. radiodurans* (DR^{WT}) cells and of a genetically engineered strain of *D. radiodurans* expressing HU-mCherry from its endogenous locus (DR^{HUmCh}) (Supplementary Figure S1A). Imaging was performed on bacteria in both exponential and early stationary growth phases (Figure 1A). In DR^{HUmCh}, HU-mCherry covers the genomic DNA and serves as a proxy to follow changes in the organization of the nucleoid (Supplementary Figure S1A). As reported previously, the mean volume of DR^{HUmCh} nucleoids is slightly higher than that of DR^{WT} (Supplementary Figure S2B), possibly as a result of steric hindrance caused by the mCherry label (8). For both strains, we evaluated the fraction of rounded nucleoids, and determined the volume and sphericity of individually segmented Syto9-labeled nucleoids, so as to perform a thorough statistical comparison of exponential versus stationary phase populations. We were particularly interested in following the relative changes in nucleoid size and morphology rather than defining absolute values, which are likely overestimated (by ~20%) due to blur of the diffraction-limited imaging. We found that in stationary phase, almost 90% of cells exhibited a rounded nucleoid (Supplementary Figure S3) and the mean nucleoid volume was decreased by almost 50% compared to that in exponential phase, going from 1.01 ± 0.34 μm^3 to 0.53 ± 0.19 μm^3 (Figure 1B). The sphericity, in contrast, increased significantly (+12%) and displayed a markedly reduced distribution in stationary phase (Figure 1B), confirming that the nucleoid morphology is much more homogeneous in this growth phase. Similar observations were made on the DR^{HUmCh} strain with a 40% drop in the nucleoid volume and a significant increase in the sphericity (Figure 1B).

Next, we compared the dynamics of HU in exponential and stationary phase cells by single-particle tracking (spt; Supplementary Figure S4A). For this, we constructed a *D. radiodurans* strain expressing HU fused to mEos4b (71), DR^{HUmEos} (Supplementary Figure S1A), enabling the characterization of HU dynamics (Figure 1C–E). PALM imaging of this strain revealed the same variety of nucleoid shapes as seen by confocal microscopy in exponential phase and a similar change in nucleoid morphology upon entering stationary phase (Figure 1E). We plotted the apparent diffusion coefficient (D_{app}) values calculated from the mean square jump distance of 4 displacements per track in exponential and stationary phase cells (Figure 1C), and extracted the median D_{app} per cell (Figure 1D). We observed that nucleoid rounding and compaction upon entry into stationary phase was accompanied by a marked reduction in the diffusion of HU, with an almost 20% lower D_{app} than that observed in exponential phase cells, suggesting a major reorganization of the HU-DNA assembly in these highly condensed nucleoids. We chose not to fit the spt data to distinct populations of molecules as reported in several earlier studies (51,52,72), since simulations revealed that such an analysis would likely be biased by the strong and heterogeneous confinement encountered by HU molecules in the various nucleoid morphologies observed in *D. radiodurans*. A detailed discussion of this issue is provided in the supplementary data (Supplementary discussion).

Western blot analysis of HU levels in cell extracts of DR^{WT}, DR^{HUmCh} and DR^{HUmEos} revealed that HU levels were unchanged upon transition from exponential to stationary phase (Figure 1F and Supplementary Figure S5). However, we observed that when fused to either mCherry or mEos4b, the levels of HU in untreated cultures were higher than in DR^{WT} despite being expressed from the same genomic locus (Supplementary Figure S6). As discussed in the supplementary data (Supplementary note), considering the similar response of the three strains to UV-C exposure, we do not expect this difference in HU expression to substantially change the function and properties of HU in genome organization.

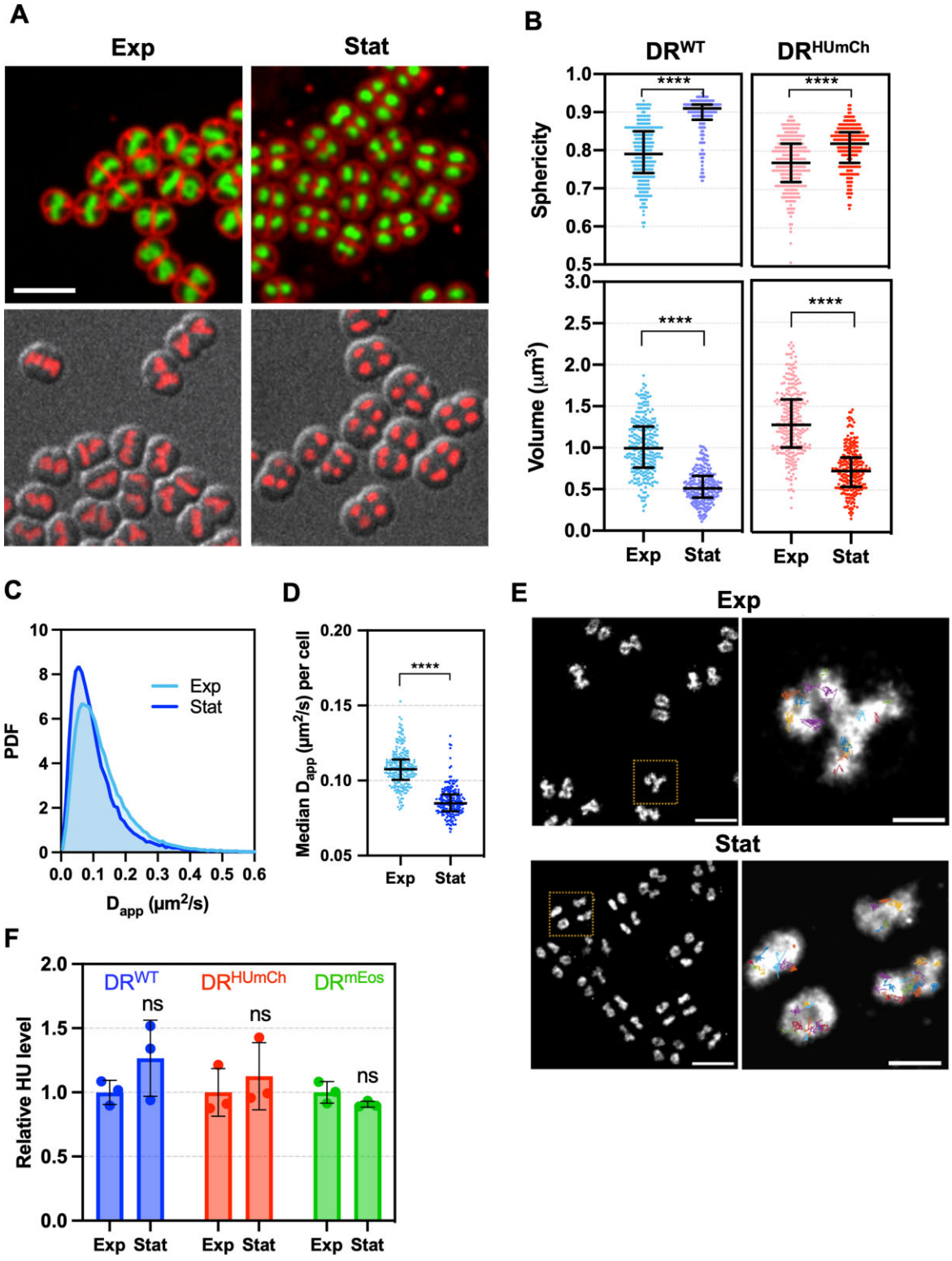

Figure 1. Growth phase-dependent nucleoid remodeling and associated changes in HU dynamics. (**A**) Representative images of DR^{WT} cells (upper panels) stained with Syto 9 and Nile Red and DR^{HUmCh} (lower panels) in exponential (left) and stationary (right) phase. Scale bar: 5 μm. (**B**) Nucleoid volume and sphericity of DR^{WT} (blue) and DR^{HUmCh} (red) strains in exponential (light color) and stationary phase (dark color) cells (n = 250). Error bars represent the median and interquartile range. **** $P < 0.0001$, Kruskal–Wallis statistical test performed in GraphPad Prism 8. (**C**) Histogram distribution of the apparent diffusion coefficient (D_{app}) of HU-mEos4b in exponential (light blue; $n = 231$) and stationary (dark blue; $n = 196$) phase DR^{HUmEos} cells. PDF: Probability density function. (**D**) Median D_{app} of HU-mEos4b per cell in exponential (light blue; $n = 231$) and stationary phase (dark blue; $n = 196$) cells. Error bars represent the median and interquartile range. **** $P < 0.0001$, Kruskal–Wallis statistical test performed in GraphPad Prism 8. (**E**) Representative images of exponential (left) and stationary (right) phase DR^{HUmEos} nucleoids. The right panel is a close up view of the boxed cells in the left panel and individual HU-mEos4b tracks are overlayed on the epi-fluorescence image. Scale bar left panel: 0.5 μm. Scale bar right panel: 3 μm. (**F**) Relative levels of HU, HU-mCherry and HU-mEos4b in exponential (Exp) and stationary (Stat) DR^{WT} (blue), DR^{HUmCh} (red) and DR^{HUmEos} (green) cells. ns: non-significant, uncorrected one-way ANOVA statistical test performed in GraphPad Prism 8.

UV-C light elicits a rapid dose-dependent compaction of the nucleoid

D. radiodurans is known to exhibit an outstanding resistance to UV light (73–75). We exposed exponential and stationary phase DR^{WT} cultures to a range of UV-C doses. Up to 1.9 kJ/m^2, the survival of *D. radiodurans* was largely unaffected, but rapidly dropped beyond this dose, regardless of whether cells were in exponential or stationary phase (Figure 2A). In contrast, survival of *E. coli* under the same experimental conditions was severely impacted already at a dose of 0.2 kJ/m^2. The UV resistance of DR^{HUmCh} and DR^{HUmEos} strains was similar to that of DR^{WT}, with between 30 and 50% cell survival at the sublethal dose of 1.9 kJ/m^2 and <0.01% survival at the lethal dose of 12.0 kJ/m^2 (Supplementary Figure S2C).

UV-C-induced changes in nucleoid volume and morphology were then evaluated by 3D spinning-disk microscopy, as described above, after irradiation of *D. radiodurans*. Due to the time needed for sample preparation, images were typically acquired 30 minutes after irradiation (cf. Materials and Methods). A dose-dependent compaction of the nucleoid of exponentially growing DR^{WT} and DR^{HUmCh} was observed up to 1.9 kJ/m^2 (Figure 2B, C and Supplementary Figures S7 and S8) reaching a minimal volume of 0.65 μm^3 for DR^{WT} and 1.11 μm^3 for DR^{HUmCh}, corresponding to respectively a 35% and 18% decrease in the mean nucleoid volume. As in the case of stationary phase cells, this nucleoid compaction was accompanied by an increased sphericity and a marked reduction in the spread of the sphericity values, suggesting the formation of more compact and homogeneous nucleoids in the cell population (Figure 2B-C and Supplementary Figures S7 and S8). Of note, in DR^{WT}, beyond the sublethal dose of 1.9 kJ/m^2, the nucleoid volume remained constant at its minimal value, whereas the mean sphericity seemed less affected by the higher UV-C doses, suggesting that nucleoid rounding might be partly impaired at these highly cytotoxic UV-C doses (Figure 2B-C and Supplementary Figures S7 and S8). The same experiments were then performed on stationary DR^{WT} and DR^{HUmCh} cultures. While no further nucleoid compaction was observed for DR^{WT} stationary phase nucleoids following exposure to UV-C light, the volume of stationary phase DR^{HUmCh} nucleoids did show a significant dose-dependent reduction going from 0.74 μm^3 in non-irradiated samples to 0.39 μm^3 in response to 12.0 kJ/m^2 (Figure 2B, C and Supplementary Figures S7B and S8B). This difference may be explained by the different levels of compaction of stationary phase nucleoids in the two strains before irradiation.

Having established the global changes in nucleoid shape and size following exposure to UV-C light, we next examined the effects of sublethal (1.9 kJ/m^2) and lethal (12.0 kJ/m^2) doses of UV-C radiation on HU diffusion using the DR^{HUmEos} strain. We first ensured that UV-C illumination did not compromise the fluorescence properties of mEos4b; only a small reduction (5–10%) in green fluorescence intensity was observed after exposure to UV-C (Supplementary Figure S2A). Although UV-C induced a clear compaction of the nucleoids as in cells entering stationary phase (Supplementary Figure S9), we observed that UV-C instead led to a significant increase in the D_{app} of HU in irradiated cells (at both sublethal and lethal doses) in both exponential and stationary phase cells (Figure 2D, E). In exponential cells, the median D_{app} of HU-mEos4b in irradiated cells was approximately twice that measured in non-irradiated samples, while in stationary phase cells, HU diffusion was ∼30% higher after irradiation. The more compact structure of stationary phase nucleoids may be more restrictive for HU diffusion.

To determine whether the increased HU diffusion observed after exposure to UV-C light could be due to increased mobility of the genomic DNA as a result of UV-induced DNA damage, we probed the mobility of the *OriC* and *Ter* loci of chromosome 1 (the largest chromosome of *D. radiodurans*, corresponding to ∼80% of the genome) by spt using a heterologous *parS*-ParB system (Supplementary Figure S10A-B) previously used to track these loci in *D. radiodurans* cells (8,76). Exponentially growing *D. radiodurans* strains in which either *OriC* or *Ter* were labelled with ParB-GFP were thus irradiated with a sublethal dose of UV-C light and imaged after 1 hour of recovery. No noticeable changes in the mobility of chromosome 1 loci were observed after exposure to UV-C light (Supplementary Figure S10C, D), suggesting that changes in HU diffusion do not result from increased mobility of the damaged DNA.

We also examined whether HU levels changed after exposure to UV-C by quantifying the abundance of HU in all three *D. radiodurans* strains 1 hour after exposure to a sublethal UV-C dose. Western blot analysis revealed that HU levels remained unchanged after irradiation (Figure 2F and Supplementary Figure S5), suggesting that the increased apparent diffusion of HU probably reflects altered HU-DNA interactions.

Cell and nucleoid recovery after a sublethal dose of UV-C light involves three distinct stages

To decipher the different stages of UV-C-induced nucleoid remodeling, we carried out a detailed analysis of the response of exponentially growing *D. radiodurans* cells to a sublethal dose of UV-C light up to 24h following irradiation (Figures 3 and 4, and Supplementary Figures S11- S14). For this purpose, irradiated cells (DR^{WT}, DR^{HUmCh} and DR^{HUmEos}) were transferred back into fresh medium immediately after irradiation and samples were then collected at different timepoints and subjected to a variety of measurements: (i) optical density measurements to determine growth curves after irradiation, (ii) 3D spinning-disk microscopy on DR^{WT} and DR^{HUmCh} to assess cell growth and division, and follow changes in size and morphology of the nucleoids, and (iii) spt experiments on DR^{HUmEos} cells to probe the mobility of HU. Before carrying out these analyses, we confirmed that the three strains of *D. radiodurans* responded in a similar way to exposure to UV-C light by establishing their growth curves and determining the size and morphology of their nucleoids at selected timepoints after irradiation (Supplementary Figure S11).

The recovery of *D. radiodurans* bacteria exposed to a sublethal (SL) UV-C dose can be divided into three main stages: stage 1^{SL} (t_0 to t_{1h} post-irradiation) during which cell growth and division are arrested and the nucleoids become round and more condensed, stage 2^{SL} (t_{1h} to t_{7h} post-irradiation) corresponding to nucleoid decompaction and a progressive recovery of cellular activity in the cell population, and stage 3^{SL} (t_{7h} to t_{24h} post-irradiation) in which most cells have recovered native nucleoid and cell morphologies (Supplementary Table S3). Optical density measurements performed on DR^{WT}, DR^{HUmCh} and DR^{HUmEos} strains exposed to a sublethal dose of UV-C light showed a clear arrest of their cell cycle immediately after irradiation causing a 2–3 h delay in their growth curve

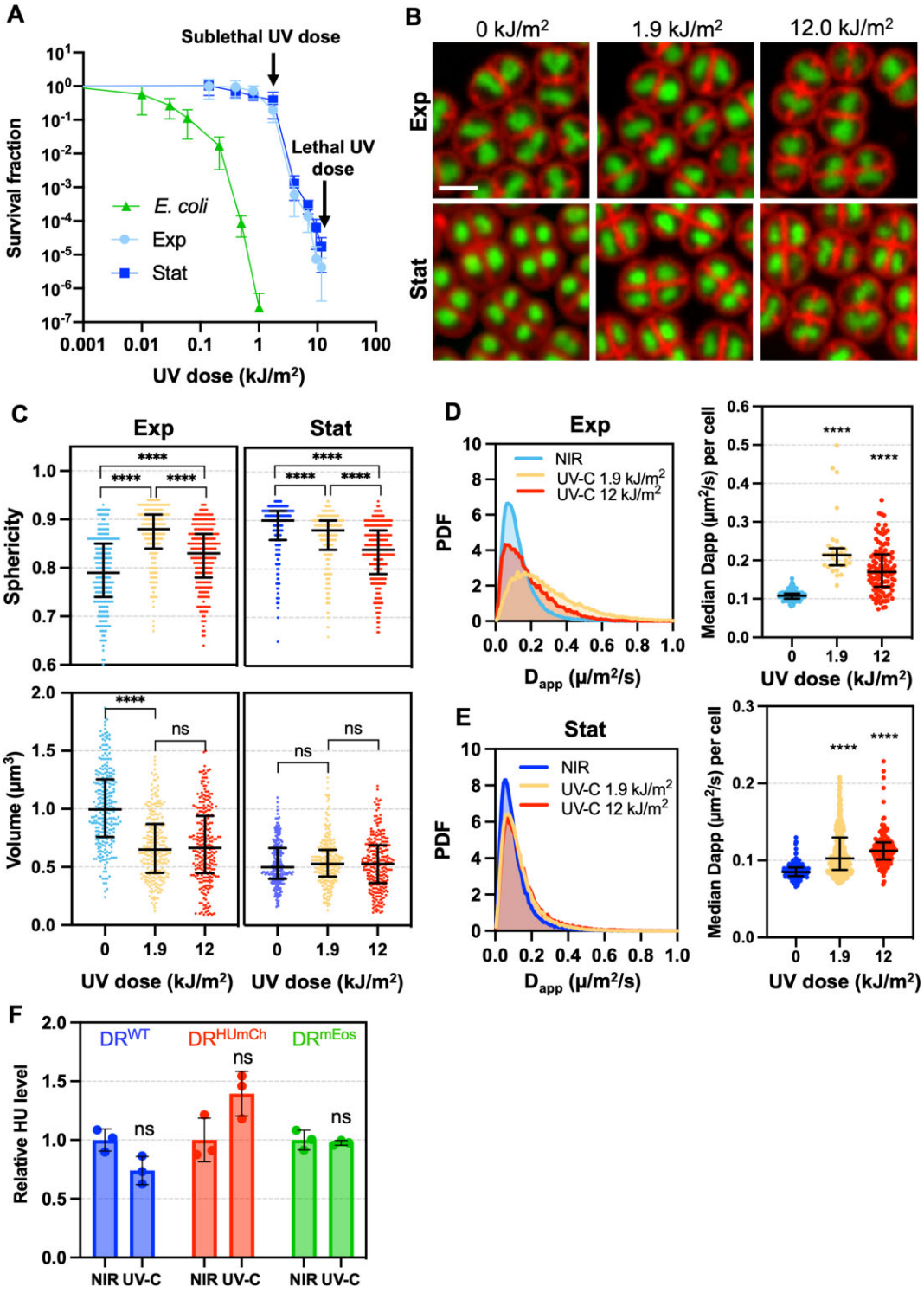

Figure 2. Dose-dependent effects of UV-C light on nucleoid organization. (**A**) Survival curves of exponential (light blue) and stationary (dark blue) phase DR^{WT} and *E. coli* (green) at different UV doses. The sublethal (1.9 kJ/m^2) and lethal (12.0 kJ/m^2) doses used for the subsequent studies are indicated with arrows. Data represent the mean and standard deviation of at least three independent experiments. (**B**) Representative images of exponential (top panel) and stationary phase (lower panel) DR^{WT} cells stained with Syto9 and Nile Red before (0 kJ/m^2; left) and after exposure to 1.9 (middle) or 12.0 kJ/m^2 (right) UV-C light. Scale bar: 2.5 µm. (**C**) Nucleoid volume and sphericity of exponential (left) and stationary (right) phase DR^{WT} cells before (0 kJ/m^2; blue) and after exposure to 1.9 (orange) or 12.0 kJ/m^2 (red) UV-C light (n = 250). Error bars represent the median and interquartile range. ns: non-significant, **** $P < 0.0001$, Kruskal–Wallis statistical test performed in GraphPad Prism 8. (**D**, **E**) Histogram distributions (left panels) of the apparent diffusion coefficient (D_{app}) of HU-mEos4b and median D_{app} (right panels) of HU-mEos4b per cell in exponential (D) and stationary (E) DR^{HUmEos} cells before (blue; $n = 231$ for exp and 196 for stat) and after exposure to 1.9 (orange; $n = 32$ for exp and 356 for stat) or 12.0 kJ/m^2 (red; $n = 114$ for exp and 152 for stat) UV-C light. PDF: Probability density function. Error bars represent the median and interquartile range. **** $P < 0.0001$, Kruskal–Wallis statistical test performed in GraphPad Prism 8. (**F**) Relative levels of HU, HU-mCherry and HU-mEos4b in non-irradiated and UV-irradiated (with 1.9 kJ/m^2 dose; after 1 h of recovery t_{1h}) DR^{WT} (blue), DR^{HUmCh} (red) and DR^{HUmEos} (green) cells. ns: non-significant, uncorrected one-way ANOVA statistical test performed in GraphPad Prism 8.

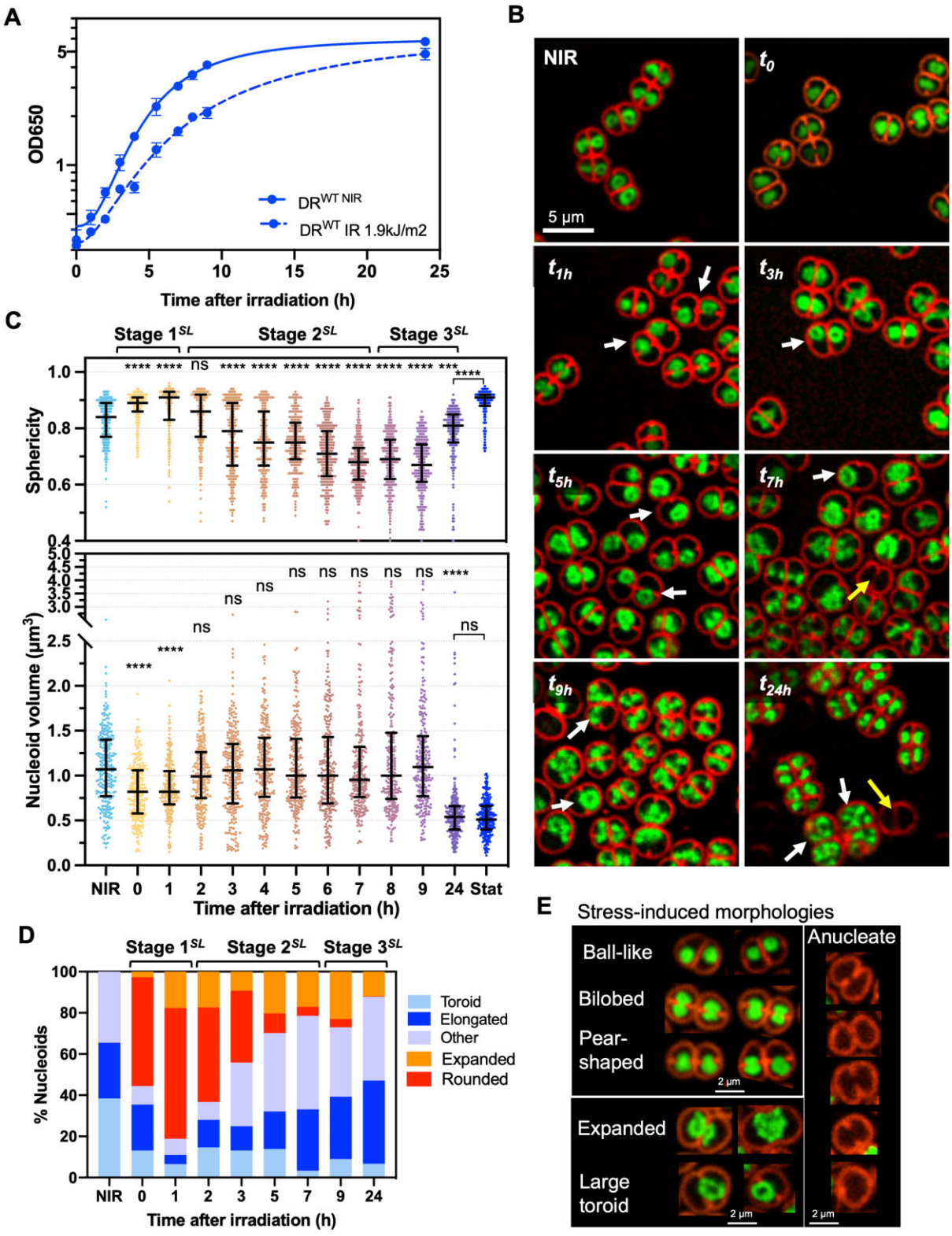

Figure 3. Effects of sublethal UV-C exposure on nucleoid organization and morphology. (**A**) Growth curves of non-irradiated (NIR; full line) and irradiated DR^{WT} (1.9 kJ/m^2; dashed line). Data represent the mean and standard deviation of at least 3 independent experiments. (**B**) Representative images of DR^{WT} cells stained with Syto9 and Nile Red at different timepoints after exposure to 1.9 kJ/m^2 UV-C light. White and yellow arrows indicate cells with off-center nucleoids and anucleate cells respectively. Scale bar: 5 µm. (**C**) Nucleoid volume and sphericity of DR^{WT} cells at different timepoints after exposure to 1.9 kJ/m^2 UV-C light ($n = 250$). Error bars represent the median and interquartile range. ns: non-significant, **** $P < 0.0001$, Kruskal–Wallis statistical test performed in GraphPad Prism 8. (**D**) Evolution of nucleoid morphologies during the recovery from exposure to 1.9 kJ/m^2 UV-C light ($n > 450$). (C, D) The three different stages of the recovery phase are indicated above the plots. (**E**) Examples of the most common UV-C-induced nucleoid and cell morphologies observed by confocal microscopy of Syto9 and Nile Red stained DR^{WT} cells after exposure to 1.9 kJ/m^2 UV-C light. In (D), rounded nucleoids correspond to ball-like, bilobed and pear-shaped nucleoids, while expanded nucleoids refer to both expanded and large toroids as depicted in (**E**).

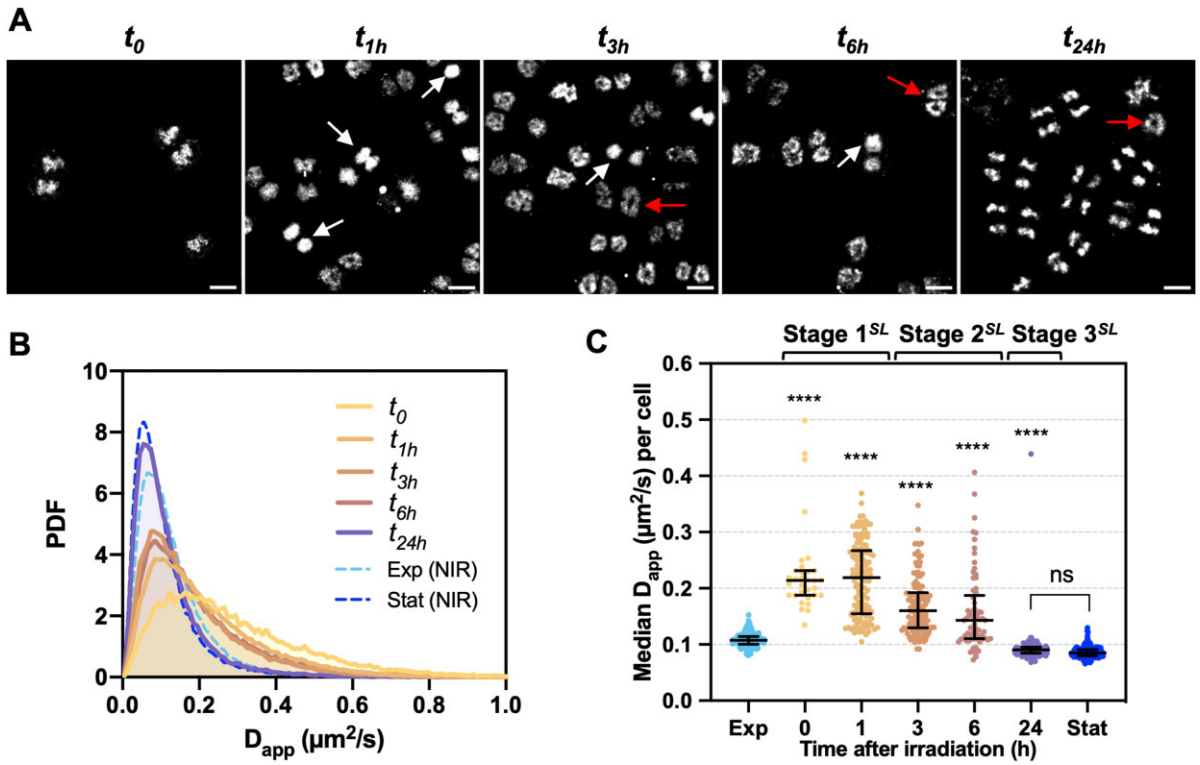

Figure 4. Effects of sublethal UV-C exposure on the mobility of HU. (**A**) Representative images of DR^{HUmEos} nucleoids at different timepoints after exposure to 1.9 kJ/m^2 UV-C light. White and red arrows indicate rounded and expanded nucleoids respectively. Scale bar: 2 µm. (**B**) Histogram distribution of the apparent diffusion coefficient (D_{app}) of HU-mEos4b in non-irradiated stationary DR^{HUmEos} (dashed blue line) cells and at different timepoints after exposure to 1.9 kJ/m^2 UV-C light (orange to purple; $n > 30$). PDF: Probability density function. (**C**) Median D_{app} of HU-mEos4b per cell in non-irradiated exponential (light blue) and stationary (dark blue) DR^{HUmEos} cells and at different timepoints after exposure to 1.9 kJ/m^2 UV-C light (orange to purple; $n > 30$). Error bars represent the median and interquartile range. ns: non-significant, **** $P < 0.0001$, Kruskal–Wallis statistical test performed in GraphPad Prism 8. The three different stages of the recovery phase are indicated above the plot.

(Figure 3A and Supplementary Figure S11B), which is in good agreement with the time estimated in earlier studies to allow cells to repair the heavy radiation-induced DNA damage (77). We indeed observed that in DR^{WT} both septation and cell growth were rapidly blocked after irradiation and throughout stage 1^{SL} of recovery. As a result, transition from phase 3 to phase 4 of the cell cycle, corresponding to the onset of septation, was impaired, leading to an increased fraction of phase 3 cells in the population at the end of stage 1^{SL} (t_{1h}; Supplementary Figure S13A-C). Interestingly, the splitting of tetrads into diads (transition from phase 6 to phase 1; Supplementary Figure S13A) did not appear to be affected by the irradiation, as evidenced by a significant reduction in the proportion of phase 6 cells during stage 1^{SL} (Supplementary Figure S12B). No obvious defects in cell morphology were seen in this first stage (Figure 3B).

Arrest of the cell cycle immediately after irradiation was accompanied by a marked reduction in the size of the nucleoid, constituting the first step in the nucleoid remodeling process (Figure 3B–D for DR^{WT} and Supplementary Figure S12 for DR^{HUmCh}). The minimal nucleoid volume was reached already at t_0 (Figure 3C and Supplementary Figure S12A), while the change in nucleoid morphology was found to progress more slowly throughout stage 1^{SL} to reach its maximum at t_{1h} with the highest median sphericity value (0.91) and near 80% of cells exhibiting abnormal nucleoid morphologies, of which 75% were rounded (Figure 3B–D and Supplementary Figure S12B and S14A). Remarkably, the nucleoids of phase 5 cells (last phase before cytokinesis) responded differently to those of other cells, with almost 50% of phase 5 cells maintaining a structured, elongated nucleoid at t_{1h} (Supplementary Figure S14B), suggesting that nucleoid compaction may be less efficient in cells in which chromosome segregation is already well advanced. Nucleoid rounding resulted in different nucleoid morphologies depending on the phase of the cell cycle the cells were in when exposed to UV-C light (Figure 3E, Supplementary Figure S14C). A majority of cells in early phases of the cell cycle (phases 1–3) bearing mostly crescent-shaped and ring-shaped nucleoids exhibited ball-like nucleoids after irradiation, whereas cells at later stages of the cell cycle (phases 4–5) in which active chromosome segregation was taking place, exhibited bilobed or pear-shaped nucleoids after irradiation (Figure 3E and Supplementary Figure S14C). Moreover, irrespective of their phase of the cell cycle, over 30% of cells exhibited off-center nucleoids at the end of stage 1^{SL} (Figure 3B and Supplementary Figure S14D), in contrast with healthy *D. radiodurans* cells in which the nucleoid is always located in the center of the cell, except immediately after chromosome segregation in phases 5 and 6 (8). Spt analysis revealed that HU diffusion also rapidly increased after irradiation, reaching a maximum at the end of stage 1 (t_{1h}; Figure 4A–C).

In stage 2^{SL} (t_{1h} to t_{7h} post-irradiation; Supplementary Table S3), HU mobility was found to progressively decrease again (Figure 4B-C). This coincided with the start of the reversal of the nucleoid compaction process. As with compaction,

the first step in nucleoid decompaction was the recovery of a 'normal' nucleoid volume as early as t_{2h} (Figure 3C and Supplementary Figure S12A), whereas full recovery of the diverse nucleoid shapes typical of exponentially growing *D. radiodurans* cells took several hours and most of stage 2^{SL} (Figure 3D and Supplementary Figure S14A and D). Nucleoid decompaction was also accompanied by a progressive decrease in the median sphericity of nucleoids and a marked increase in the spread of the sphericity values, reflecting the great diversity of nucleoid shapes observed during the recovery stage, most likely resulting from active DNA repair and other cell recovery processes (Figure 3C and Supplementary Figure S12A).

Cell growth and division were also largely recovered during stage 2^{SL} as illustrated by the increased optical density of DR^{WT}, DR^{HUmCh} and DR^{HUmEos} cultures (Figure 3A and Supplementary Figure S11B) and a restored distribution of cells within the different phases of the cell cycle (Supplementary Figure S13B). A slow increase in the mean cell size was nonetheless observed between t_{1h} and t_{3h}, which may have resulted from a slight delay between the recovery of cell growth and that of cell division (Supplementary Figure S13C). Beyond t_{3h}, most cells appeared to have recovered their ability to grow and divide and the mean cell size decreased progressively as the cell density increased and the bacterial population moved towards stationary phase. However, we also observed during this period the accumulation of a small fraction (<5%) of anucleate cells (i.e. no Syto9 staining; Figure 3B and E and Supplementary Figure S14D) that typically also exhibited a damaged cell membrane (discontinuous Nile Red staining), and a significant number (~10% cells) of abnormally large cells in which cell division appeared to be impaired or blocked (Figure 3B and E and Supplementary Figure S14E). Many of these enlarged cells also exhibited abnormally large nucleoids that were either spread out throughout the cell and exhibited significantly increased volumes or forming very large rings with a largely unchanged nucleoid volume (Figure 3C–E and Supplementary Figure S14F). These cells were likely more severely damaged, causing a delay or even an arrest in the nucleoid remodeling process.

In stage 3^{SL} of the recovery from a sublethal dose of UV-C light (t_{7h} to t_{24h} post-irradiation; Supplementary Table S3), a vast majority of cells had fully recovered and exhibited normal growth and division as evidenced by the rapid increase in the optical densities of the cultures (Figure 3A and Supplementary Figure S11B) and the changes in cell phase distribution as the cells shifted from exponential to stationary phase (Figure 3A, B and Supplementary Figure S13B). Indeed, at t_{24h} post-irradiation, these cultures had reached early stationary phase as seen by the accumulation of phase 6–8 cells (Figure 3B, Figure 4A and Supplementary Figures S12B and S13B). Most cells (80–90%) now exhibited normal, structured and centered nucleoids (Figure 3D and Supplementary Figure S14D). During stage 3^{SL}, HU diffusion continued its recovery to reach values under 0.1 $\mu m^2/s$ as obtained in non-irradiated stationary phase cells (Figure 4B, C and Figure 1E). Surprisingly, however, at the end of stage 3^{SL}, around 10% of cells still exhibited major defects (large cells with impaired septation, expanded nucleoids and high HU diffusion), suggesting that these large, abnormal cells appeared to still arise at late stages of recovery, likely as a result of unrepaired DNA damage leading to cell dysfunctions (Figure 3B–E, Figure 4A and C, and Supplementary Figure S12B).

A lethal dose of UV-C light induces a progressive loss of nucleoid structure and cellular functions

We then subjected our three exponentially growing *D. radiodurans* strains (DR^{WT}, DR^{HUmCh} and DR^{HUmEos}) to a lethal (L) dose of UV-C light and followed the effects of this high dose on the cells and their nucleoids in the hours following irradiation (Figures 5 and 6, and Supplementary Figure S15-S16). As with the sublethal dose, all three strains responded in a similar manner (Supplementary Figure S15A, B) and the recovery could also be divided into three stages, but the nature and duration of these stages differed from those observed after exposure to sublethal UV-C. After a lethal UV-C dose, rapid nucleoid rounding and condensation were also observed in stage 1^L (t_0 to t_{2h} post-irradiation; Supplementary Table S3), but this process lasted longer than after the sublethal dose. Indeed, while a reversal of nucleoid compaction was observed at t_{1h} (corresponding to the onset of stage 2^{SL}) after a sublethal dose, instead, in the case of a lethal dose, we noted that after the rapid condensation of the nucleoids immediately after irradiation, the mean nucleoid volume (~0.75 μm^3) then remained constant for the rest of stage 1^L until t_{2h} (Figure 5B, C and Supplementary Figures S15A and S16A). The change in nucleoid morphology was also more progressive with the highest sphericity (>0.9) reached at t_{2h} (Figure 5B-C and Supplementary Figures S15A and S16A). With this higher dose of UV-C, 100% of cells exhibited abnormal nucleoids with ~95% of cells exhibiting rounded nucleoids and 50% of cells having off-center nucleoids at t_{2h} (Figure 5B–D and Supplementary Figure S16B). These values are considerably higher than those determined for cells exposed to the sublethal dose (Figure 3D and Supplementary Figure S14D). During stage 1^L, HU-mEos4b diffusion strongly increased, beyond the value obtained for the sublethal dose with a very large cell-to-cell variation observed at t_{1h} (Figure 6A–C). As expected, cell growth and division were rapidly arrested after this acute UV-C dose as evidenced by the flat growth curve of DR^{WT}, DR^{HUmCh} and DR^{HUmEos} cultures (Figure 5A and Supplementary Figure S15B) and the stable cell size during stage 1^L (Supplementary Figure S15C).

Whereas nucleoid compaction was reversed in stage 2^{SL} after the sublethal dose, no such reversal was seen after the lethal dose. Instead, during stage 2^L (t_{2h} to t_{9h} post-irradiation; Supplementary Table S3), evidence for severe cellular dysfunction was observed: (i) lack of cell growth (Supplementary Figure S15C), (ii) increased fraction of cells exhibiting off-center nucleoids (Figure 5B and Supplementary Figure S16B), (iii) accumulation of anucleate cells with reduced size due to a damaged cell wall (up to ~25% of cells at t_{7h}; Figure 5B and D), (iv) high levels of HU diffusion (Figure 6A–C) and (v) progressive reduction in the size of rounded nucleoids leading to the accumulation of micro-nucleoids with a mean volume of 0.27 μm^3 corresponding to a 75% reduction in the nucleoid volume compared to non-irradiated samples (Figure 5E).

In stage 3^L (t_{9h} to t_{24h} post-irradiation; Supplementary Table S3), there is a marked accumulation of cells exhibiting either no or diffuse staining of the DNA, suggesting that for a vast majority of cells, the integrity of the nucleoid was severely affected and genomic DNA was being heavily degraded (Figure 5B-D and Supplementary Figure S16). Indeed, at t_{24h}, 95% of cells showed either no Syto9-DNA staining (40% of anucleate cells) or diffuse Syto9-DNA staining throughout the cytosol (55%). In accordance with this, HU

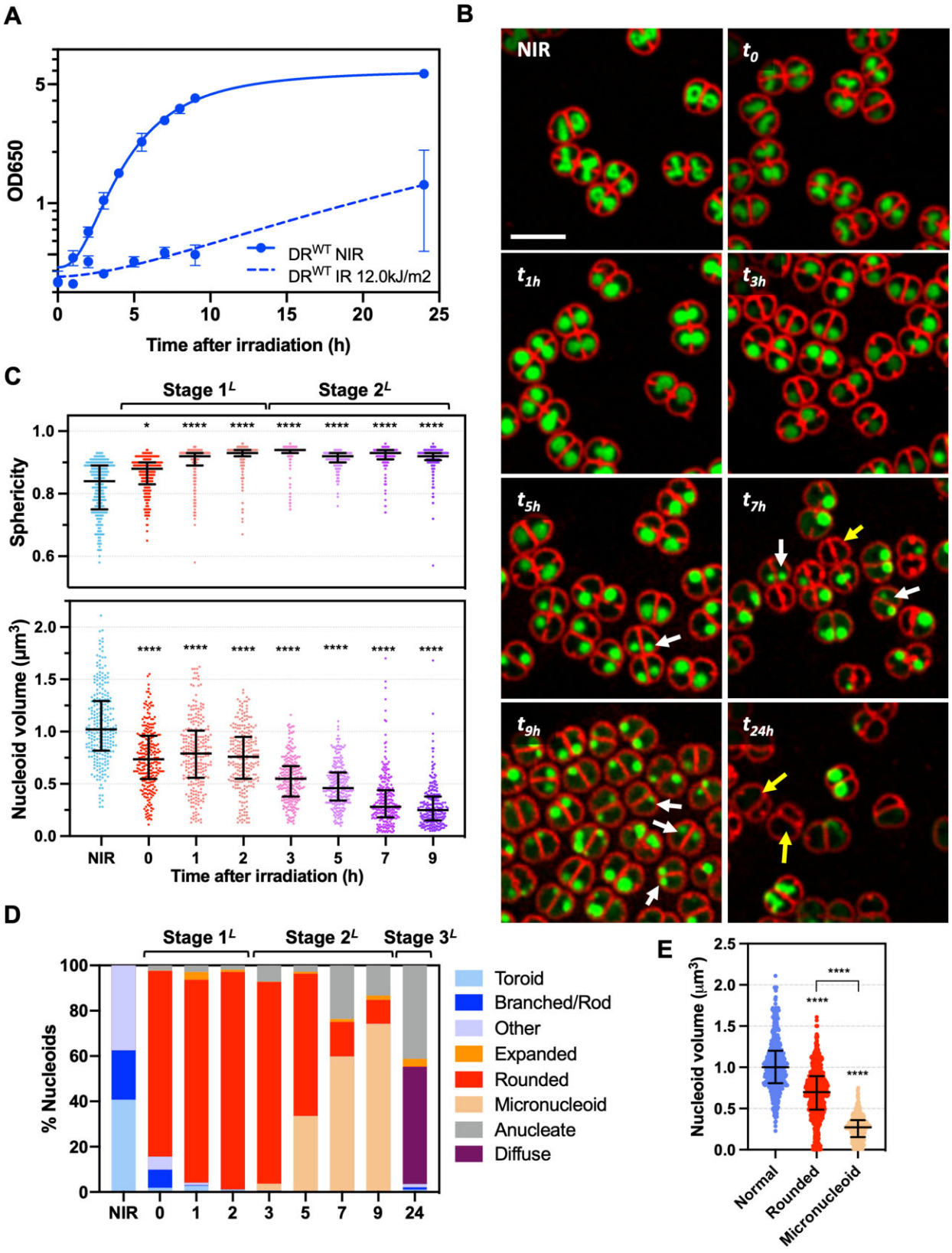

Figure 5. Effects of lethal UV-C exposure on nucleoid organization and morphology. (**A**) Growth curves of non-irradiated (NIR; full line) and irradiated DR^{WT} (12.0 kJ/m^2; dashed line). Data represent the mean and standard deviation of at least 3 independent experiments. (**B**) Representative images of DR^{WT} cells stained with Syto9 and Nile Red at different timepoints after exposure to 12.0 kJ/m^2 UV-C light. White and yellow arrows indicate cells with micro-nucleoids and anucleate cells respectively. Scale bar: 5 µm. (**C**) Nucleoid volume and sphericity of DR^{WT} cells at different timepoints after exposure to 12.0 kJ/m^2 UV-C light (n = 250). Error bars represent the median and interquartile range. * $P < 0.05$, **** $P < 0.0001$, Kruskal–Wallis statistical test performed in GraphPad Prism 8. (**D**) Evolution of nucleoid morphologies during the recovery from exposure to 12.0 kJ/m^2 UV-C light ($n > 450$). (C, D) The different stages of the response phase are indicated above the plots. (**E**) Nucleoid volumes associated with different nucleoid morphologies ($n > 400$). **** $P < 0.0001$, Kruskal–Wallis statistical test performed in GraphPad Prism 8.

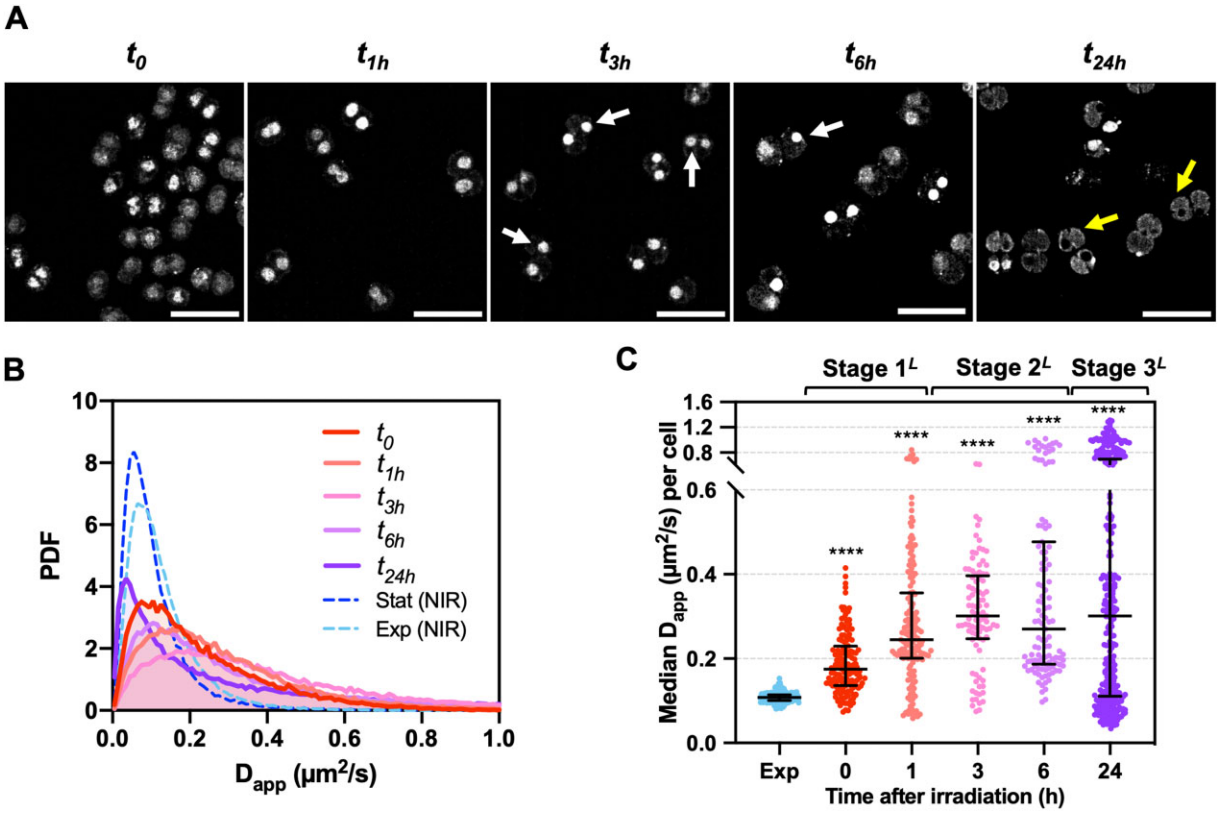

Figure 6. Effects of lethal UV-C exposure on the mobility of HU. (**A**) Representative images of DR^{HUmEos} nucleoids at different timepoints after exposure to 12.0 kJ/m^2 UV-C light. White and yellow arrows indicate micronucleoids and diffuse nucleoids respectively. Scale bar: 5 μm. (**B**) Histograms of the apparent diffusion coefficient (D_{app}) of HU-mEos4b in non-irradiated exponential DR^{HUmEos} (dashed blue line) cells and at different timepoints after exposure to 12.0 kJ/m^2 UV-C light (red to purple; $n > 37$). (**C**) Median D_{app} of HU-mEos4b per cell in non-irradiated exponential (light blue) DR^{HUmEos} cells and at different timepoints after exposure to 12.0 kJ/m^2 UV-C light (red to purple; $n > 37$). Error bars represent the median and interquartile range. **** $P < 0.0001$, Kruskal–Wallis statistical test performed in GraphPad Prism 8. The three different stages of the response phase are indicated above the plot.

diffusion remained at a high level throughout stages 2^L and 3^L, with many cells showing D_{app} values close or above 1 μm^2/s, confirming the probable release of HU from the degraded genomic DNA in these cells (Figure 6A–C). Strikingly, there was also a substantial fraction of cells in which HU diffusion was very low ($D_{app} < 0.1$ μm^2/s), possibly as a result of protein aggregation (Figure 6C). Extensive DNA degradation was also evidenced in Syto9-stained DR^{HUmCh} cells, where an increasing number of HU-mCherry positive and Syto9 negative nucleoids were seen to accumulate during stage 3^L (Supplementary Figure S17).

Discussion

In this study, we have investigated nucleoid remodeling in *D. radiodurans* in response to two different types of stress: (i) entry into stationary phase, which is associated with nutritional stress and (ii) exposure to UV-C light, which is known to cause severe DNA damage. A comparison of the response to these two types of stress (Figure 7) provides important insight into the mechanisms underlying bacterial nucleoid remodeling.

In both cases, nucleoids rapidly became more compact and changed their morphology to adopt a more rounded shape. Upon entry into stationary phase, strong nucleoid compaction was accompanied by a significant decrease in HU diffusion, but no significant change in HU abundance, suggesting that the available HU is binding more tightly, and perhaps in a different configuration, to the genomic DNA compared to exponentially growing cells (Figure 7). Indeed, a marked reduction in the volume of stationary phase nucleoids is likely to result in an increased local concentration of HU in the vicinity of the DNA, which in turn may modify the DNA binding properties of HU and favor the formation of HU-DNA assemblies in which HU polymerizes along the genomic DNA, thereby stiffening and bundling the genomic DNA. A similar model was recently proposed by Hammel and colleagues for *E. coli* HU in stationary phase (6,48). This model is also supported by *in vitro* atomic force microscopy studies of DrHU-plasmid DNA assemblies, in which stiffening and bridging of plasmid DNA by DrHU were observed at high HU:DNA ratios only (39) and would explain the reduced apparent diffusion of HU observed in the highly condensed stationary phase *D. radiodurans* nucleoids. By maintaining this condensed genomic configuration in stationary phase, HU also likely affects the transcription of stationary phase specific genes required for survival under resource-limited growth conditions as has been reported in *E. coli* (11,78,79).

As in stationary phase cells, exposure of *D. radiodurans* cells to UV-C light rapidly induced nucleoid compaction, although to a lesser extent, and this phenomenon was again associated with changes in HU mobility regardless of the UV dose. However, while HU diffusion was decreased in stationary phase cells, it was significantly increased in response to UV-C light (Figure 7). The structure of condensed stationary

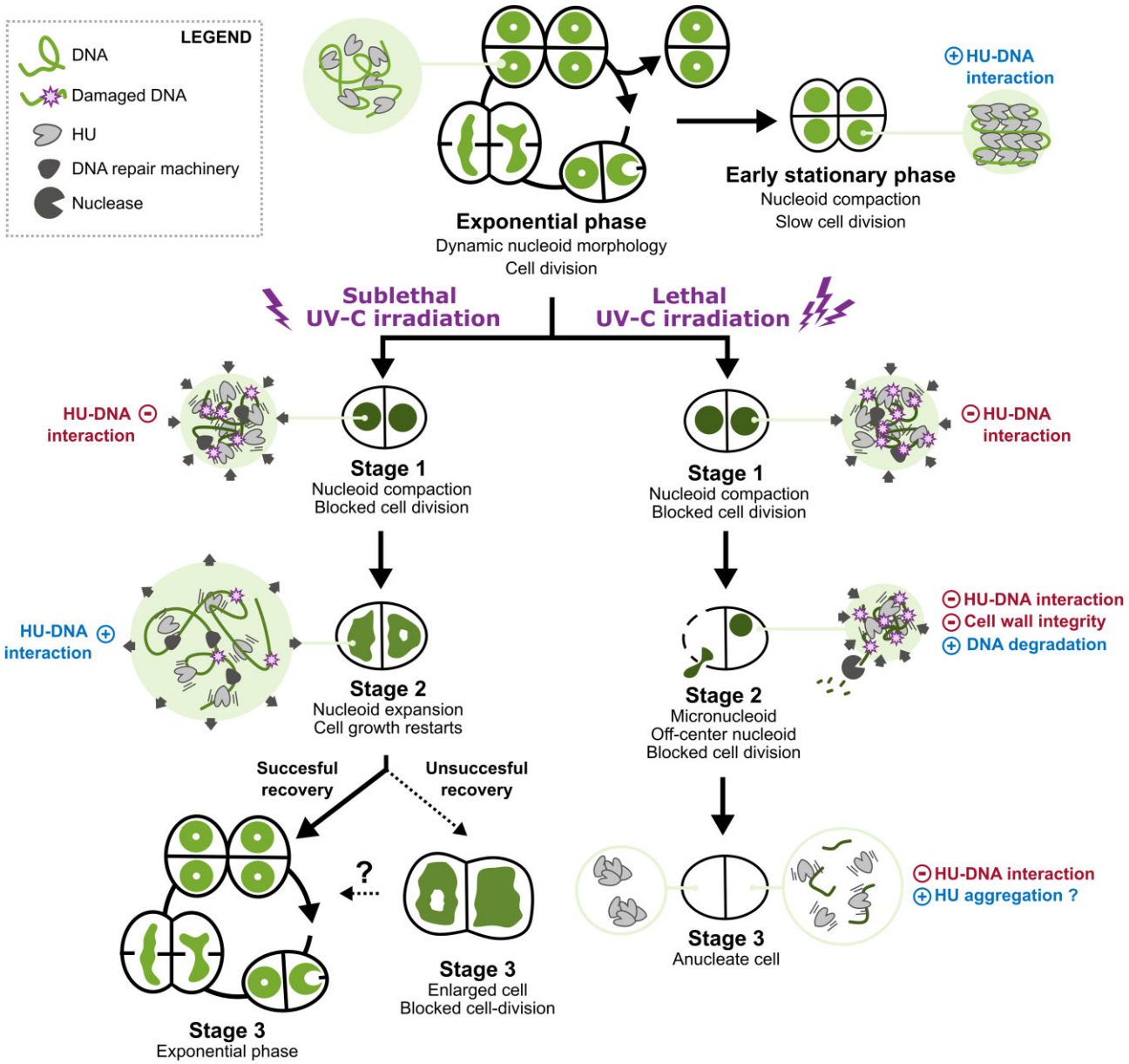

Figure 7. Model of stress-induced nucleoid remodeling in *D. radiodurans*. Schematic diagram summarizing the main stages of nucleoid remodeling in *D. radiodurans* induced by either entry into stationary phase (top right) or by exposure to either sublethal (lower left) or lethal (lower right) doses of UV-C irradiation. Changes in nucleoid size and shape are notably accompanied by significant variations in the diffusion of the HU protein, likely reflecting altered HU-DNA interactions. Nucleoid remodeling is also tightly coordinated with cell growth and division.

phase nucleoids is thus distinct from that of UV-C-irradiated nucleoids, although in both cases, HU-DNA interactions are likely playing an important role in the underlying organization. Increased mobility of the irradiated genomic DNA due to DNA damage could have been one of the causes of the observed increased HU dynamics, but the tracking of the *oriC* and *ter* loci of the major chromosome of *D. radiodurans* showed no evidence for a substantial change in DNA mobility after exposure to UV-C light. Similarly, increased levels of HU in the cell, and more particularly DNA-free HU, could also lead to an increased apparent diffusion coefficient for HU, but here again, no significant changes in the total levels of HU were detected following exposure to UV-C light. The increased HU diffusion thus probably results from weakened HU-DNA interactions induced by either post-translational modifications and/or physico-chemical changes occurring at the level of HU and/or the genomic DNA, directly induced by the high-intensity UV-C light and the overproduction of ROS (80,81).

A major consequence of HU release from the genomic DNA as a result of weakened HU-DNA interactions could be compaction or collapse of the nucleoid, although additional factors are likely also involved in this phenomenon. UV-induced arrest (or partial arrest) of cellular processes, including cell growth and division, but also DNA replication and transcription or protein translation, which are known to induce changes in nucleoid organization (82,83), is likely to also contribute to this rapid stress-induced nucleoid condensation. Similarly, reduced transcription and translation as well as severe damage to the bacterial cytoskeleton network may be responsible for the subsequent drift of nucleoids off-center, that was particularly striking in cells exposed to lethal UV-C

light (Figure 7). Using theoretical approaches, Marc Joyeux showed that bacterial nucleoids preferentially locate to the edges of the cell, where the curvature of the cell wall is the highest (84), suggesting that in healthy cells active cellular processes, including transcription and translation (83), are indeed responsible for maintaining the nucleoid in a central position. These processes are likely impaired in the strongly irradiated cells, causing the nucleoid to lose its structure and drift to the edge of the cell.

A major difference in the response of *D. radiodurans* to sublethal versus lethal UV-C doses was the reversibility of the process. In *D. radiodurans* cells exposed to sublethal UV-C light, the rapid initial nucleoid compaction stage (stage 1^{SL}) was followed by a slower decompaction phase (stage 2^{SL}) during which the nucleoids progressively recovered their well-structured states and cells recovered their ability to grow and divide. HU is likely to play an important role in this recovery stage. We, indeed, observed that the kinetics of recovery of nucleoid morphology after exposure to sublethal UV-C light coincided with that of recovery of HU dynamics, suggesting that progressive re-assembly of HU on the genomic DNA is an important determinant of nucleoid organization and may be critical for regulating access of DNA repair enzymes to the genomic DNA. On the contrary, a lethal dose of UV-C light lead to progressive loss of nucleoid structure in stage 2^{L}, heavy degradation of the genomic DNA, full arrest of cell growth and division, and eventually to the accumulation of damaged and anucleate cells in stage 3^{L}. In such cells, HU diffusion was found to be either very high, indicating that HU–DNA interactions were largely disrupted, or instead very low, possibly as a result of HU aggregation in the absence of genomic DNA on which to assemble.

Cell survival is thus essential to restore nucleoid organization following exposure to UV-C light and in contrast to nucleoid condensation which may be a mostly passive process, nucleoid decompaction, and more generally cell recovery, largely relies on active cellular processes (Figure 7). In particular, active checkpoint control factors must be functional to rapidly coordinate the arrest of the cell cycle and chromosome segregation with the intervention of the DNA repair machinery to restore the integrity of the genome. A similar sequential compaction and expansion of nucleoids was reported in UV-C irradiated *E. coli* cells before cell division could restart (85,86). Obsbu and Skarstad proposed that the initial phase of compaction serves to stabilize the DNA and repair DNA double-strand breaks, while repair of other lesions takes place largely during the decompaction stage (85). In *D. radiodurans*, nucleoid condensation appears to occur regardless of the nature of the stress and its intensity, suggesting that it may constitute an early stress response mechanism, which could act mostly as a protective measure to minimize dispersion of the damaged genome. Earlier studies have shown that activation of the DNA repair machinery occurs 30 to 60 minutes after exposure to radiation (87,88), suggesting that most of the repair process would therefore take place during the early stages of decompaction (start of stage 2^{SL}), before full reassembly of HU on the genomic DNA. This hypothesis is in line with studies in eukaryotic cells showing that the chromatin decondenses in response to DNA damage to facilitate repair (89,90). The 2–3h delay in the growth of *D. radiodurans* after exposure to UV-C is also in good agreement with this hypothesis and the estimated time needed to allow cells to repair heavy radiation-induced DNA damage (77).

In *D. radiodurans*, although many cells recovered well from exposure to the sublethal UV-C dose and started to grow and divide again during stage 2^{SL} of the recovery phase, a fraction of cells exhibited highly expanded nucleoids. These cells were typically larger in size and lacking a division septum, suggesting that they had recovered their ability to grow, but not to divide. Castro *et al.* showed that *E. coli* cells that are deficient in DNA repair proteins reach the expanded nucleoid stage, but are unable to restart cell division after UV-C irradiation, suggesting that DNA repair is required before cell division can restart (86). *D. radiodurans* cells exhibiting highly expanded nucleoids were thus probably either failing to repair their DNA damage or delayed in their repair process, leading to arrested cell division and partial loss of their nucleoid organization. A fraction of such cells may eventually recover and start dividing again after completion of the repair process. Interestingly, such cells arose progressively during the recovery, suggesting that cells that initially appeared to have recovered subsequently developed cellular defects probably as a consequence of accumulated DNA damage.

In conclusion, this study provides a first detailed view of the different stages of stress-induced nucleoid remodeling in *D. radiodurans* and highlights the key role of HU and the versatility of its interactions with genomic DNA in this process and more generally in the survival strategy of this remarkable organism. In the future, combining live cell fluorescence imaging of NAPs with label-free imaging techniques, such as soft X-ray tomography on intact bacteria or cryo-electron tomography on focused-ion beam (FIB)-milled lamella, to visualize the ultra-structure of the nucleoid, will certainly provide a more in-depth view of the intricate mechanisms underlying this complex process. In addition, besides HU, we expect additional NAPs to contribute to this nucleoid remodeling process. These include DdrC, a *Deinococcus*-specific NAP that is strongly up-regulated in response to irradiation (91,92), the partitioning factors (ParA/ParB) or the DNA gyrase, all of which are known to be recruited to the nucleoid after irradiation (38), but also new factors that remain to be identified, notably through the characterization of the interactome of major NAPs such as HU. Finally, a number of recent studies have revealed the importance of post-translational modifications of NAPs for regulating the activities and DNA-binding properties of these small basic proteins, so in the future, establishing the post-translational modification profiles of key NAPs at different stages of the nucleoid remodeling process will certainly shed new light on the underlying mechanisms.

Data availability

The data underlying this article are available in the supplementary information (data presented in the various plots) or will be shared on reasonable request to the corresponding author.

Supplementary data

Supplementary Data are available at NAR Online.

Acknowledgements

We thank Claire Bouthier de la Tour for help in the preparation of the genetically engineered strain of *D. radiodurans* and Salvatore De Bonis for purifying HU-mCherry. IBS acknowl-

edges integration into the Interdisciplinary Research Institute of Grenoble (IRIG, CEA).

Funding

CEA Radiobiology program; J.W.'s PhD position was funded by GRAL, a project of the University Grenoble Alpes graduate school (Ecoles Universitaires de Recherche) CBH-EUR-GS [ANR-17-EURE-0003]; Agence Nationale de la Recherche [ANR-20-CE11-0013-01, ANR-22-CE11-0029-01]; M4D imaging platform of the Grenoble Instruct-ERIC Center (ISBG: UMS 3518 CNRS-CEA-UGA-EMBL) within the Grenoble Partnership for Structural Biology (PSB), supported by FRISBI [ANR-10-INBS-05-02]; GRAL [ANR-10-LABX-49-01], financed within the University Grenoble Alpes graduate school (Ecoles Universitaires de Recherche) CBH-EUR-GS [ANR-17-EURE-0003]. The open access publication charge for this paper has been waived by Oxford University Press — *NAR* Editorial Board members are entitled to one free paper per year in recognition of their work on behalf of the journal.

Conflict of interest statement

None declared.

References

1. Dame,R.T., Rashid,F.-Z.M. and Grainger,D.C. (2020) Chromosome organization in bacteria: mechanistic insights into genome structure and function. *Nat. Rev. Genet.*, **21**, 227–242.
2. Hołówka,J. and Zakrzewska-Czerwińska,J. (2020) Nucleoid associated proteins: the small organizers that help to cope with stress. *Front. Microbiol.*, **11**, 590.
3. Steil,L., Serrano,M., Henriques,A.O. and Völker,U. (2005) Genome-wide analysis of temporally regulated and compartment-specific gene expression in sporulating cells of *Bacillus subtilis*. *Microbiology (Reading)*, **151**, 399–420.
4. Kar,S., Edgar,R. and Adhya,S. (2005) Nucleoid remodeling by an altered HU protein: Reorganization of the transcription program. *Proc. Natl. Acad. Sci. U.S.A.*, **102**, 16397–16402.
5. Mitosch,K., Rieckh,G. and Bollenbach,T. (2019) Temporal order and precision of complex stress responses in individual bacteria. *Mol. Syst. Biol.*, **15**, e8470.
6. Remesh,S.G., Verma,S.C., Chen,J.-H., Ekman,A.A., Larabell,C.A., Adhya,S. and Hammel,M. (2020) Nucleoid remodeling during environmental adaptation is regulated by HU-dependent DNA bundling. *Nat. Commun.*, **11**, 2905.
7. Meyer,A.S. and Grainger,D.C. (2013) The *Escherichia coli* Nucleoid in Stationary Phase. In: *Advances in Applied Microbiology*. Elsevier, Vol. **83**, pp. 69–86.
8. Floc'h,K., Lacroix,F., Servant,P., Wong,Y.-S., Kleman,J.-P., Bourgeois,D. and Timmins,J. (2019) Cell morphology and nucleoid dynamics in dividing *Deinococcus radiodurans*. *Nat. Commun.*, **10**, 3815.
9. Szafran,M.J., Jakimowicz,D. and Elliot,M.A. (2020) Compaction and control—the role of chromosome-organizing proteins in *Streptomyces*. *FEMS Microbiol. Rev.*, **44**, 725–739.
10. Piggot,P.J. and Hilbert,D.W. (2004) Sporulation of *Bacillus subtilis*. *Curr. Opin. Microbiol.*, **7**, 579–586.
11. Hengge,R. (2011) Stationary-phase gene regulation in *Escherichia coli*. *EcoSal Plus*, **4**, https://doi.org/10.1128/ecosalplus.5.6.3.
12. Chawla,M., Mishra,S., Anand,K., Parikh,P., Mehta,M., Vij,M., Verma,T., Singh,P., Jakkala,K., Verma,H.N., *et al.* (2018) Redox-dependent condensation of the mycobacterial nucleoid by WhiB4. *Redox. Biol.*, **19**, 116–133.
13. Morikawa,K., Ushijima,Y., Ohniwa,R.L., Miyakoshi,M. and Takeyasu,K. (2019) What happens in the Staphylococcal nucleoid under oxidative stress? *Microorganisms*, **7**, 631.
14. Shechter,N., Zaltzman,L., Weiner,A., Brumfeld,V., Shimoni,E., Fridmann-Sirkis,Y. and Minsky,A. (2013) Stress-induced condensation of bacterial genomes results in re-pairing of sister chromosomes. *J. Biol. Chem.*, **288**, 25659–25667.
15. Zimmerman,J.M. and Battista,R.J. (2005) A ring-like nucleoid is not necessary for radioresistance in the Deinococcaceae. *BMC Microbiol.*, **5**, 17–27.
16. Dillon,S.C. and Dorman,C.J. (2010) Bacterial nucleoid-associated proteins, nucleoid structure and gene expression. *Nat. Rev. Micro.*, **8**, 185–195.
17. Verma,S.C., Qian,Z. and Adhya,S.L. (2019) Architecture of the *Escherichia coli* nucleoid. *PLoS Genet.*, **15**, e1008456.
18. Azam,T.A. and Ishihama,A. (1999) Twelve Species of the Nucleoid-associated Protein from *Escherichia coli*. *J. Biol. Chem.*, **274**, 33105–33113.
19. Macvanin,M. and Adhya,S. (2012) Architectural organization in *E. coli* nucleoid. *Biochim. Biophys. Acta (BBA) - Gene Regul. Mech.*, **1819**, 830–835.
20. Gupta,M., Sajid,A., Sharma,K., Ghosh,S., Arora,G., Singh,R., Nagaraja,V., Tandon,V. and Singh,Y. (2014) HupB, a nucleoid-associated protein of *Mycobacterium tuberculosis*, is modified by serine/threonine protein kinases *in vivo*. *J. Bacteriol.*, **196**, 2646–2657.
21. Ghosh,S., Padmanabhan,B., Anand,C. and Nagaraja,V. (2016) Lysine acetylation of the *Mycobacterium tuberculosis* HU protein modulates its DNA binding and genome organization. *Mol. Microbiol.*, **100**, 577–588.
22. Okanishi,H., Kim,K., Fukui,K., Yano,T., Kuramitsu,S. and Masui,R. (2017) Proteome-wide identification of lysine succinylation in thermophilic and mesophilic bacteria. *Biochim. Biophys. Acta (BBA) - Proteins Proteomics*, **1865**, 232–242.
23. Dilweg,I.W. and Dame,R.T. (2018) Post-translational modification of nucleoid-associated proteins: an extra layer of functional modulation in bacteria? *Biochem. Soc. Trans.*, **46**, 1381–1392.
24. Nair,S. and Finkel,S.E. (2004) Dps protects cells against multiple stresses during stationary phase. *J. Bacteriol.*, **186**, 4192–4198.
25. Haikarainen,T. and Papageorgiou,A.C. (2010) Dps-like proteins: structural and functional insights into a versatile protein family. *Cell. Mol. Life Sci.*, **67**, 341–351.
26. Sato,Y.T., Watanabe,S., Kenmotsu,T., Ichikawa,M., Yoshikawa,Y., Teramoto,J., Imanaka,T., Ishihama,A. and Yoshikawa,K. (2013) Structural change of DNA induced by nucleoid proteins: growth phase-specific Fis and stationary phase-specific Dps. *Biophys. J.*, **105**, 1037–1044.
27. Karas,V.O., Westerlaken,I. and Meyer,A.S. (2015) The DNA-binding protein from starved cells (Dps) utilizes dual functions to defend cells against multiple stresses. *J. Bacteriol.*, **197**, 3206–3215.
28. Cossa,A., Trépout,S., Wien,F., Groen,J., Le Brun,E., Turbant,F., Besse,L., Pereiro,E. and Arluison,V. (2022) Cryo soft X-ray tomography to explore *Escherichia coli* nucleoid remodeling by Hfq master regulator. *J. Struct. Biol.*, **214**, 107912.
29. Boor,K.J. (2006) Bacterial stress responses: what doesn't kill them can make them stronger. *PLoS Biol.*, **4**, e23.
30. Boutte,C.C. and Crosson,S. (2013) Bacterial lifestyle shapes stringent response activation. *Trends Microbiol.*, **21**, 174–180.
31. Makarova,K.S., Aravind,L., Wolf,Y.I., Tatusov,R.L., Minton,K.W., Koonin,E.V. and Daly,M.J. (2001) Genome of the extremely radiation-resistant bacterium *Deinococcus radiodurans* viewed from the perspective of comparative genomics. *Microbiol. Mol. Biol. Rev.*, **65**, 44–79.
32. Cox,M.M. and Battista,J.R. (2005) *Deinococcus radiodurans* - the consummate survivor. *Nat. Rev. Microbiol.*, **3**, 882–892.
33. Krisko,A. and Radman,M. (2013) Biology of extreme radiation resistance: the way of *Deinococcus radiodurans*. *Cold Spring Harb. Perspect. Biol.*, **5**, a012765.

34. Timmins,J. and Moe,E. (2016) A decade of biochemical and structural studies of the DNA repair machinery of *Deinococcus radiodurans*. *Comput. Struct. Biotechnol. J.*, **14**, 168–176.
35. Ott,E., Kawaguchi,Y., Kölbl,D., Chaturvedi,P., Nakagawa,K., Yamagishi,A., Weckwerth,W. and Milojevic,T. (2017) Proteometabolomic response of *Deinococcus radiodurans* exposed to UVC and vacuum conditions: initial studies prior to the Tanpopo space mission. *PLoS One*, **12**, e0189381.
36. Ott,E., Kawaguchi,Y., Kölbl,D., Rabbow,E., Rettberg,P., Mora,M., Moissl-Eichinger,C., Weckwerth,W., Yamagishi,A. and Milojevic,T. (2020) Molecular repertoire of *Deinococcus radiodurans* after 1 year of exposure outside the International Space Station within the Tanpopo mission. *Microbiome*, **8**, 150.
37. Horne,W.H., Volpe,R.P., Korza,G., DePratti,S., Conze,I.H., Shuryak,I., Grebenc,T., Matrosova,V.Y., Gaidamakova,E.K., Tkavc,R., *et al.* (2022) Effects of desiccation and freezing on microbial ionizing radiation survivability: considerations for Mars sample return. *Astrobiology*, **22**, 1337–1350.
38. Bouthier de la Tour,C., Passot,F.M., Toueille,M., Mirabella,B., Guerin,P., Blanchard,L., Servant,P., de Groot,A., Sommer,S. and Armengaud,J. (2013) Comparative proteomics reveals key proteins recruited at the nucleoid of *Deinococcus* after irradiation-induced DNA damage. *Proteomics*, **13**, 3457–3469.
39. Chen,S.W.W., Banneville,A.S., Teulon,J.M., Timmins,J. and Pellequer,J.L. (2020) Nanoscale surface structures of DNA bound to: *Deinococcus radiodurans* HU unveiled by atomic force microscopy. *Nanoscale*, **12**, 22628–22638.
40. Romao,C.V., Mitchell,E.P. and McSweeney,S. (2006) The crystal structure of *Deinococcus radiodurans* Dps protein (DR2263) reveals the presence of a novel metal centre in the N terminus. *J. Biol. Inorg. Chem.*, **11**, 891–902.
41. Cuypers,M.G., Mitchell,E.P., Romao,C.V. and McSweeney,S.M. (2007) The crystal structure of the Dps2 from *Deinococcus radiodurans* reveals an unusual pore profile with a non-specific metal binding site. *J. Mol. Biol.*, **371**, 787–799.
42. Nguyen,H.H., de la Tour,C.B., Toueille,M., Vannier,F., Sommer,S. and Servant,P. (2009) The essential histone-like protein HU plays a major role in *Deinococcus radiodurans* nucleoid compaction. *Mol. Microbiol.*, **73**, 240–252.
43. Santos,S.P., Mitchell,E.P., Franquelim,H.G., Castanho,M.A., Abreu,I.A. and Romao,C.V. (2015) Dps from *Deinococcus radiodurans*: oligomeric forms of Dps1 with distinct cellular functions and Dps2 involved in metal storage. *FEBS J.*, **282**, 4307–4327.
44. Santos,S.P., Yang,Y., Rosa,M.T.G., Rodrigues,M.A.A., De La Tour,C.B., Sommer,S., Teixeira,M., Carrondo,M.A., Cloetens,P., Abreu,I.A., *et al.* (2019) The interplay between Mn and Fe in *Deinococcus radiodurans* triggers cellular protection during paraquat-induced oxidative stress. *Sci. Rep.*, **9**, 17217.
45. Beaufay,F., Amemiya,H.M., Guan,J., Basalla,J., Meinen,B.A., Chen,Z., Mitra,R., Bardwell,J.C.A., Biteen,J.S., Vecchiarelli,A.G., *et al.* Polyphosphate drives bacterial heterochromatin formation. *Sci. Adv.*, **7**, eabk0233.
46. Stojkova,P., Spidlova,P. and Stulik,J. (2019) Nucleoid-Associated Protein HU: A Lilliputian in Gene Regulation of Bacterial Virulence. *Front. Cell. Infect. Microbiol.*, **9**, 159.
47. Grove,A. (2011) Functional evolution of bacterial histone-like HU proteins. *Curr. Iss. Mol. Biol.*, **13**, 1–12.
48. Hammel,M., Amlanjyoti,D., Reyes,F.E., Chen,J.H., Parpana,R., Tang,H.Y.H., Larabell,C.A., Tainer,J.A. and Adhya,S. (2016) HU multimerization shift controls nucleoid compaction. *Sci. Adv.*, **2**, e1600650.
49. Salerno,P., Larsson,J., Bucca,G., Laing,E., Smith,C.P. and Flärdh,K. (2009) One of the two genes encoding nucleoid-associated HU proteins in *Streptomyces coelicolor* is developmentally regulated and specifically involved in spore maturation. *J. Bacteriol.*, **191**, 6489–6500.
50. Schramm,F.D. and Murray,H. (2022) HU knew? *Bacillus subtilis* HBsu is required for DNA replication initiation. *J. Bacteriol.*, **204**, e0015122.
51. Bettridge,K., Verma,S., Weng,X., Adhya,S. and Xiao,J. (2021) Single-molecule tracking reveals that the nucleoid-associated protein HU plays a dual role in maintaining proper nucleoid volume through differential interactions with chromosomal DNA. *Mol. Microbiol.*, **115**, 12–27.
52. Stracy,M., Schweizer,J., Sherratt,D.J., Kapanidis,A.N., Uphoff,S. and Lesterlin,C. (2021) Transient non-specific DNA binding dominates the target search of bacterial DNA-binding proteins. *Mol. Cell*, **81**, 1499–1514.
53. Kamashev,D. and Rouviere-Yaniv,J. (2000) The histone-like protein HU binds specifically to DNA recombination and repair intermediates. *EMBO J.*, **19**, 6527–6535.
54. Ghosh,S. and Grove,A. (2004) Histone-like protein HU from *Deinococcus radiodurans* binds preferentially to four-way DNA junctions. *J. Mol. Biol.*, **337**, 561–571.
55. Verma,S.C., Harned,A., Narayan,K. and Adhya,S. (2023) Non-specific and specific DNA binding modes of bacterial histone, HU, separately regulate distinct physiological processes through different mechanisms. *Mol. Microbiol.*, **119**, 439–455.
56. Hou,J., Dai,J., Chen,Z., Wang,Y., Cao,J., Hu,J., Ye,S., Hua,Y. and Zhao,Y. (2022) Phosphorylation Regulation of a Histone-like HU Protein from *Deinococcus radiodurans*. *Protein Pept. Lett.*, **29**, 891–899.
57. Aki,T. (1997) Repressor induced site-specific binding of HU for transcriptional regulation. *EMBO J.*, **16**, 3666–3674.
58. Oberto,J., Nabti,S., Jooste,V., Mignot,H. and Rouviere-Yaniv,J. (2009) The HU regulon is composed of genes responding to anaerobiosis, acid stress, high osmolarity and SOS induction. *PLoS One*, **4**, e4367.
59. Li,S. and Waters,R. (1998) *Escherichia coli* strains lacking protein HU are UV sensitive due to a role for HU in homologous recombination. *J. Bacteriol.*, **180**, 3750–3756.
60. Huisman,O., Faelen,M., Girard,D., Jaffé,A., Toussaint,A. and Rouvière-Yaniv,J. (1989) Multiple defects in *Escherichia coli* mutants lacking HU protein. *J. Bacteriol.*, **171**, 3704–3712.
61. Bouthier De La Tour,C., Armengaud,J., Dulermo,R., Blanchard,L., Devigne,A., De Groot,A., Ludanyi,M. and Sommer,S. (2015) The abundant and essential HU proteins in *Deinococcus deserti* and *Deinococcus radiodurans* are translated from leaderless mRNA. *Microbiology*, **161**, 2410–2422.
62. Ghosh,S. and Grove,A. (2006) The *Deinococcus radiodurans*-encoded HU protein has two DNA-binding domains. *Biochemistry*, **45**, 1723–1733.
63. Gefen,O., Fridman,O., Ronin,I. and Balaban,N.Q. (2014) Direct observation of single stationary-phase bacteria reveals a surprisingly long period of constant protein production activity. *Proc. Natl. Acad. Sci. U.S.A.*, **111**, 556–561.
64. Dworkin,J. and Harwood,C.S. (2022) Metabolic reprogramming and longevity in quiescence. *Annu. Rev. Microbiol.*, **76**, 91–111.
65. Richa,Sinha, R.P. and H Ä Der,D.P. (2015) Physiological aspects of UV-excitation of DNA. *Top. Curr. Chem.*, **356**, 203–248.
66. Mennecier,S., Coste,G., Servant,P., Bailone,A. and Sommer,S. (2004) Mismatch repair ensures fidelity of replication and recombination in the radioresistant organism *Deinococcus radiodurans*. *Mol. Genet. Genomics*, **272**, 460–469.
67. Floc'h,K., Lacroix,F., Barbieri,L., Servant,P., Galland,R., Butler,C., Sibarita,J.-B., Bourgeois,D. and Timmins,J. (2018) Bacterial cell wall nanoimaging by autoblinking microscopy. *Sci. Rep.*, **8**, 14038.
68. Stringer,C., Wang,T., Michaelos,M. and Pachitariu,M. (2021) Cellpose: a generalist algorithm for cellular segmentation. *Nat. Methods*, **18**, 100–106.
69. Schneider,C.A., Rasband,W.S. and Eliceiri,K.W. (2012) NIH Image to ImageJ: 25 years of image analysis. *Nat. Methods*, **9**, 671–675.
70. Ovesný,M., Křížek,P., Borkovec,J., Švindrych,Z. and Hagen,G.M. (2014) ThunderSTORM: A comprehensive ImageJ plug-in for

PALM and STORM data analysis and super-resolution imaging. *Bioinformatics*, **30**, 2389–2390.
71. De Zitter,E., Thédié,D., Mönkemöller,V., Hugelier,S., Beaudouin,J., Adam,V., Byrdin,M., Van Meervelt,L., Dedecker,P. and Bourgeois,D. (2019) Mechanistic investigation of mEos4b reveals a strategy to reduce track interruptions in sptPALM. *Nat. Methods*, **16**, 707–710.
72. Kapanidis,A.N., Uphoff,S. and Stracy,M. (2018) Understanding protein mobility in bacteria by tracking single molecules. *J. Mol. Biol.*, **430**, 4443–4455.
73. Harsojo,Kitayama, S. and Matsuyama,A. (1981) Genome multiplicity and radiation resistance in *Micrococcus radiodurans*. *J. Biochem.*, **90**, 877–880.
74. Battista,J.R. (1997) Against all odds: the survival strategies of *Deinococcus radiodurans*. *Annu. Rev. Microbiol.*, **51**, 203–224.
75. Slade,D. and Radman,M. (2011) Oxidative stress resistance in *Deinococcus radiodurans*. *Microbiol. Mol. Biol. Rev.*, **75**, 133–191.
76. Passot,F.M., Nguyen,H.H., Dard-Dascot,C., Thermes,C., Servant,P., Espeli,O. and Sommer,S. (2015) Nucleoid organization in the radioresistant bacterium *Deinococcus radiodurans*. *Mol. Microbiol.*, **97**, 759–774.
77. Zahradka,K., Slade,D., Bailone,A., Sommer,S., Averbeck,D., Petranovic,M., Lindner,A.B. and Radman,M. (2006) Reassembly of shattered chromosomes in *Deinococcus radiodurans*. *Nature*, **443**, 569–573.
78. Sobetzko,P., Travers,A. and Muskhelishvili,G. (2012) Gene order and chromosome dynamics coordinate spatiotemporal gene expression during the bacterial growth cycle. *Proc. Natl. Acad. Sci. U.S.A.*, **109**, E42–E50.
79. Lal,A., Dhar,A., Trostel,A., Kouzine,F., Seshasayee,A.S.N. and Adhya,S. (2016) Genome scale patterns of supercoiling in a bacterial chromosome. *Nat. Commun.*, **7**, 11055.
80. Kehrer,J.P. (2000) The Haber–Weiss reaction and mechanisms of toxicity. *Toxicology*, **149**, 43–50.
81. Díaz-Riaño,J., Posada,L., Acosta,I.C., Ruíz-Pérez,C., García-Castillo,C., Reyes,A. and Zambrano,M.M. (2019) Computational search for UV radiation resistance strategies in *Deinococcus swuensis* isolated from Paramo ecosystems. *PLoS One*, **14**, e0221540.
82. Woldringh,C.L., Jensen,P.R. and Westerhoff,H.V. (1995) Structure and partitioning of bacterial DNA: determined by a balance of compaction and expansion forces? *FEMS Microbiol. Lett.*, **131**, 235–242.
83. Miangolarra,A.M., Li,S.H.-J., Joanny,J.-F., Wingreen,N.S. and Castellana,M. (2021) Steric interactions and out-of-equilibrium processes control the internal organization of bacteria. *Proc. Natl. Acad. Sci. U.S.A.*, **118**, e2106014118.
84. Joyeux,M. (2019) Preferential localization of the bacterial nucleoid. *Microorganisms*, **7**, 204.
85. Odsbu,I. and Skarstad,K. (2014) DNA compaction in the early part of the SOS response is dependent on RecN and RecA. *Microbiology*, **160**, 872–882.
86. Estévez Castro,C.F., Serment-Guerrero,J.H. and Fuentes,J.L. (2018) Influence of uvrA, recJ and recN gene mutations on nucleoid reorganization in UV-treated *Escherichia coli* cells. *FEMS Microbiol. Lett.*, **365**, fny110.
87. Liu,Y., Zhou,J., Omelchenko,M.V., Beliaev,A.S., Venkateswaran,A., Stair,J., Wu,L., Thompson,D.K., Xu,D., Rogozin,I.B., *et al.* (2003) Transcriptome dynamics of *Deinococcus radiodurans* recovering from ionizing radiation. *Proc. Natl. Acad. Sci. U.S.A.*, **100**, 4191–4196.
88. Basu,B. and Apte,S.K. (2012) Gamma radiation-induced proteome of *Deinococcus radiodurans* primarily targets DNA repair and oxidative stress alleviation. *Mol. Cell. Proteomics*, **11**, M111.011734.
89. dos Santos,Á., Cook,A.W., Gough,R.E., Schilling,M., Olszok,N.A., Brown,I., Wang,L., Aaron,J., Martin-Fernandez,M.L., Rehfeldt,F., *et al.* (2020) DNA damage alters nuclear mechanics through chromatin reorganization. *Nucleic. Acids. Res.*, **49**, 340–353.
90. Hauer,M.H., Seeber,A., Singh,V., Thierry,R., Sack,R., Amitai,A., Kryzhanovska,M., Eglinger,J., Holcman,D., Owen-Hughes,T., *et al.* (2017) Histone degradation in response to DNA damage enhances chromatin dynamics and recombination rates. *Nat. Struct. Mol. Biol.*, **24**, 99–107.
91. Bouthier de la Tour,C., Mathieu,M., Meyer,L., Dupaigne,P., Passot,F., Servant,P., Sommer,S., Le Cam,E. and Confalonieri,F. (2017) *In vivo* and *in vitro* characterization of DdrC, a DNA damage response protein in *Deinococcus radiodurans bacterium*. *PLoS One*, **12**, e0177751.
92. Banneville,A.-S., Bouthier de la Tour,C., De Bonis,S., Hognon,C., Colletier,J.-P., Teulon,J.-M., Le Roy,A., Pellequer,J.-L., Monari,A., Dehez,F., *et al.* (2022) Structural and functional characterization of DdrC, a novel DNA damage-induced nucleoid associated protein involved in DNA compaction. *Nucleic Acids Res.*, **50**, 7680–7696.

Received: December 15, 2023. **Revised:** April 23, 2024. **Editorial Decision:** April 24, 2024. **Accepted:** April 26, 2024